



RESEARCH ARTICLE

10.1029/2017JE005467

Key Points:

- Multiple calibration and normalization methods to determine hydrogen content from the hydrogen-alpha LIBS emission line were evaluated
- O 778- and C 248-nm norms have the lowest scatter for the lab set, best correct for distance, and successfully determine H for Martian rocks
- Nonlinear calibrations for high-H samples and differences in H between rocks, when natural versus pelletized, warrant further study

Supporting Information:

- Supporting Information S1
- Data Set S1

Correspondence to:

N. H. Thomas,
nhthomas@caltech.edu

Citation:

Thomas, N. H., Ehlmann, B. L., Anderson, D. E., Clegg, S. M., Forni, O., Schröder, S., et al. (2018). Characterization of hydrogen in basaltic materials with laser-induced breakdown spectroscopy (LIBS) for application to MSL ChemCam data. *Journal of Geophysical Research: Planets*, 123, 1996–2021. <https://doi.org/10.1029/2017JE005467>

Received 15 OCT 2017

Accepted 1 JUL 2018

Accepted article online 10 JUL 2018

Published online 11 AUG 2018

©2018. The Authors.

This is an open access article under the terms of the Creative Commons Attribution-NonCommercial-NoDerivs License, which permits use and distribution in any medium, provided the original work is properly cited, the use is non-commercial and no modifications or adaptations are made.

Characterization of Hydrogen in Basaltic Materials With Laser-Induced Breakdown Spectroscopy (LIBS) for Application to MSL ChemCam Data

N. H. Thomas¹ , B. L. Ehlmann^{1,2} , D. E. Anderson¹ , S. M. Clegg³ , O. Forni⁴ , S. Schröder^{4,5}, W. Rapin¹ , P.-Y. Meslin⁴ , J. Lasue⁴ , D. M. Delapp³ , M. D. Dyar⁶ , O. Gasnault⁴ , R. C. Wiens³ , and S. Maurice⁴

¹Division of Geological and Planetary Sciences, California Institute of Technology, Pasadena, CA, USA, ²Jet Propulsion Laboratory, California Institute of Technology, Pasadena, CA, USA, ³Los Alamos National Laboratory, Los Alamos, NM, USA, ⁴Institut de Recherche en Astrophysique et Planétologie, Université de Toulouse, Toulouse, France, ⁵German Aerospace Center (DLR), Berlin, Germany, ⁶Mount Holyoke College, South Hadley, MA, USA

Abstract The Mars Science Laboratory rover, *Curiosity*, is equipped with ChemCam, a laser-induced breakdown spectroscopy (LIBS) instrument, to determine the elemental composition of nearby targets quickly and remotely. We use a laboratory sample set including prepared mixtures of basalt with systematic variation in hydrated mineral content and compositionally well-characterized, altered basaltic volcanic rocks to measure hydrogen by characterizing the H-alpha emission line in LIBS spectra under Martian environmental conditions. The H contents of all samples were independently measured using thermogravimetric analysis. We found that H peak area increases with weight percent H for our laboratory mixtures with basaltic matrices. The increase is linear with weight percent H in the mixtures with structurally bound H up to about 1.25 wt.% H and then steepens for higher H-content samples, a nonlinear trend not previously reported but potentially important for characterizing high water content materials. To compensate for instrument, environmental, and target matrix-related effects on quantification of H content from the LIBS signal, we examined multiple normalization methods. The best performing methods utilize O 778- and C 248-nm emission lines. The methods return comparable results when applied to ChemCam data of H-bearing materials on Mars. The calibration and normalization methods tested here will aid in investigations of H by LIBS on Mars with ChemCam and SuperCam. Further laboratory work will aid quantification across different physical matrices and heterogeneous textures because of differences we observed in H in pelletized and natural rock samples of the same composition.

Plain Language Summary ChemCam, one of the *Curiosity* rover instruments, measures the chemical composition of nearby targets quickly and remotely using laser-induced breakdown spectroscopy (LIBS). The LIBS technique requires laboratory calibration to quantitatively determine the abundances of major and minor elements. We measured prepared mixtures of basalt with systematic variation in hydrated mineral content and compositionally well-characterized, altered basaltic volcanic rocks with a ChemCam-analog instrument under Martian environmental conditions to characterize LIBS hydrogen emission. To compensate for instrument, environmental, and target-related effects on quantification of H content from the LIBS signal, we tested multiple normalization methods. While the H signal increased nonlinearly with weight percent for high H samples, we found laboratory calibrations that allowed us to successfully determine the H content of Martian veins and bedrock measured by ChemCam.

1. Introduction

Laser-induced breakdown spectroscopy (LIBS) provides chemical information by collecting light emitted by excited atoms, ions, and simple molecules in the plasma generated by laser vaporization of a sample. The ChemCam instrument on the *Curiosity* rover uses LIBS to determine geochemical composition and can detect the presence of light elements including hydrogen. ChemCam fires a pulsed laser beam at a rock or soil target and ablates a 350- to 550- μm diameter area (Maurice et al., 2012; Wiens et al., 2012). The emission spectrum from the plasma is recorded by the ChemCam spectrometers over the 240- to 840-nm wavelength range and used to derive elemental compositions (Wiens et al., 2013).

The Curiosity rover is investigating sedimentary rocks that are part of Aeolus Mons, informally known as Mount Sharp, an interior 5-km tall mound within 154-km diameter Gale crater. Hydrogen is a crucial element for Curiosity's characterization of past aqueous environments with liquid water and assessment of habitability. On Mars, water and OH can occur adsorbed on surfaces or in hydrated or hydroxylated minerals, including amorphous phases (Ehlmann & Edwards, 2014). Curiosity employs the Dynamic Albedo of Neutrons (DAN) instrument to assess hydrogen content in the near subsurface (decimeter scale) over a few meter-scale footprint beneath the rover (Mitrofanov et al., 2012). The Sample Analysis at Mars (SAM) instrument can detect H₂O and H₂ released from solid samples upon heating, using the combination of a quadrupole mass spectrometer, a tunable laser spectrometer, and a gas chromatograph to obtain chemical and isotopic compositions of volatiles released (Mahaffy et al., 2012). The Alpha Particle X-ray spectrometer can determine when light "missing" elements are present but cannot determine hydrogen content directly (Campbell et al., 2012). The CheMin instrument can identify crystalline minerals that host hydrogen in their structure (Blake et al., 2012). ChemCam is the only instrument that is both sensitive to hydrogen content and can simultaneously characterize the sample geochemistry at a submillimeter scale. In addition, ChemCam is a remote sensing instrument, so reconnaissance data are acquired daily and the immediate results can serve to motivate follow-up detailed analyses with the rover payload.

Determining the degree and style of aqueous alteration of rock units, including the presence of specific hydrated salts and hydrated silicates, is an important geochemical task for Curiosity and can be aided by analysis of hydrogen with ChemCam data. For example, the water or OH content of basaltic sedimentary materials is a key indicator of the extent to which they interacted with liquid water. ChemCam has demonstrated the ability to recognize hydrated mineral phases and use them for determining environmental conditions. Analysis of calcium sulfate veins in Yellowknife Bay sedimentary deposits with ChemCam identified H emission supporting hydrated forms of the salt (Nachon et al., 2014; Schröder et al., 2015) that later were determined to be bassanite (Rapin et al., 2016). In addition, H has been detected and characterized in dust and soils (Meslin et al., 2013; Schröder et al., 2014). Schröder et al. (2015) extended this work to drill tailings and rocks, making the first steps toward relative quantification of hydrogen with ChemCam while showing the dependence of the analysis on target type with higher intensities in the tailings than the rocks.

The abundances of major elements and some trace elements in ChemCam data are being quantified by univariate and multivariate modeling of database reference samples and calibration targets on board the rover (Maurice et al., 2016, and references therein). The detection of hydrogen by the 656.5 nm (wavelengths in vacuum will be used throughout this paper) LIBS emission line (H-alpha) is straightforward. Hydrogen has been detected in most of the targets observed by ChemCam (Schröder et al., 2015). Lab work has shown quantifying hydrogen content from this single line is a challenge (Sobron et al., 2012). A second H emission line at 486.13 nm is located at the edge of the ChemCam visible and near-infrared (VNIR) detector where sensitivity is too low for quantitative analysis (Schröder et al., 2015). Recent results from Rapin et al. (2016) have characterized the LIBS H emission for calcium sulfates, while Rapin et al. (2017a) studied H emission for a set of pelletized basalts, fluorhydroxyapatites, hydroxyapatites, opals, and sulfates using a ChemCam model LIBS instrument but did not measure any natural rock samples. A first absolute quantification was then proposed by Rapin et al. (2017a) that only considered a linear calibration curve.

The goal of this project is to qualitatively and quantitatively examine how hydrogen emission varies with composition and to develop calibration curves based on laboratory data, acquired under simulated Martian conditions, which may later be modified and employed to analyze ChemCam and SuperCam (Wiens et al., 2017) LIBS data from Mars. We utilize prepared mixtures of basalt with varying quantities of Mars-relevant hydrated minerals as well as compositionally well-characterized natural, altered basaltic rocks. Some of our samples contain structural H₂O or structural OH, and their H₂O contents and release temperatures were independently determined using thermogravimetric analysis (TGA). Our work builds on previous studies by Rapin et al. (2017a) and others by introducing new measurements to study the quantification of hydrogen within a basaltic matrix for a larger set of Mars-relevant hydrated materials, important for characterizing chemical matrix effects. We test a variety of normalization techniques for LIBS H to develop a calibration based on our sample set. Our study examines whether the calibration curves remain linear at

Table 1
List of All Samples and Mixtures

Sample	Chemical formula	Number of samples or mixtures	Sample origin	Sample source	Years measured (20XX)	Mixture Number ^a
K1919	Basalt	1	Near USGS BHVO-1 locality in Kilauea, Hawaii	Caltech collection	13, 14, 15	
GBW07105 (GBW)	Basalt	1	NRCCRM, China	Brammer	14, 17	
Iceland basalts	rock compositions in Ehlmann et al., 2012	6 samples	Hvalfjordur and Berfjordur, Iceland	Ehlmann et al., 2012	13, 15	
San Carlos basanites	rock compositions in Hadnott et al., 2017	7 samples	San Carlos, AZ	Hadnott et al., 2017	13, 15	
Ca Chloride	CaCl ₂	6–K1919	Synthetic, reagent grade	J.T. Baker	13	5
Na Chloride	NaCl	6–K1919 and GBW	Synthetic, reagent grade	Macron Chemicals	13, 14, 17	1, 14
Calcite (Ca Carbonate)	CaCO ₃	6–K1919	Minas, Nuevo Leon, Mexico	Ward's	13	2
Magnesite (Mg Carbonate)	MgCO ₃	7–K1919	unknown	Ward's	14, 17	7
Gypsum	CaSO ₄ · 2H ₂ O	6–K1919 and GBW	Fremont County, Colorado	Ward's	13, 14, 17	3, 13
Fe (III) Sulfate	Fe ₂ (SO ₄) ₃	7–K1919	Synthetic, reagent grade	Carolina Chemical	14, 17	10
Mg Sulfate	MgSO ₄	7–K1919	Synthetic, reagent grade	Macron Chemicals	14, 17	8
Na Sulfate	Na ₂ SO ₄	7–K1919	Synthetic, reagent grade	Carolina Chemical	14, 17	11
Quartz	SiO ₂	6–K1919	NW end of Saline Valley, CA	Caltech mineral collection	13	4
Opal	SiO ₂ · nH ₂ O	7–K1919	Colton, San Bernadino Co., CA	Caltech mineral collection	14, 17	12
Hematite	Fe ₂ O ₃	6–K1919	Joan Monlevade, Minas Gerias, Brazil	Caltech mineral collection	13	6
NAu-1	(Ca,Na,K) _{1.05} (Si _{6.98} Al _{1.02}) (Al _{0.29} Fe _{3.68} Mg _{0.04})O ₂₀ (OH) ₄	7–K1919	South Australia	Keeling et al., 2000	15	15
NAu-2	(Ca,Na,K) _{0.72} (Si _{7.55} Al _{0.45}) (Fe _{3.83} Mg _{0.05})O ₂₀ (OH) ₄	7–K1919	South Australia	Keeling et al., 2000	15	16
Alunite (with clay mineral impurities)	KAl ₃ (SO ₄) ₂ (OH) ₆	7–K1919	Utah	Ward's	14, 17	9
Brucite	Mg(OH) ₂	7–K1919	Gabbs, NV	Caltech mineral collection	15	17
Epidote	Ca ₂ Fe _{2.25} Al _{0.75} (SiO ₄) ₃ (OH)	7–K1919	Rockbridge CO., VA	Caltech mineral collection	15	20
Muscovite	KAl ₂ (AlSi ₃ O ₁₀)(F,OH) ₂	7–K1919	Upson County, GA	Caltech mineral collection	15	18
Serpentine	((Mg,Fe) ₃ Si ₂ O ₅ (OH) ₄	7–K1919	Hoboken, NJ	Caltech mineral collection	15	19

^aLabeling key for our supplementary data set available online and for the Los Alamos National Laboratory calibration data set used for the ChemCam data available on the Planetary Data System.

high weight percent H. We also present LIBS results for a set of natural rocks, which have not been studied in previous laboratory studies, to begin characterization of physical matrix effects related to grain size, sample roughness, and cohesion. We test our methods by applying to ChemCam data to identify the range of hydration of sulfate veins and estimate the hydration of the Martian bedrock at Gale crater.

2. Samples and Methods

2.1. Samples

To characterize LIBS H emission, we created a sample set including both prepared mixtures of basalt with Mars-relevant minerals in varied proportions and compositionally well-characterized altered volcanics (Table 1).

2.1.1. Mixtures

The wide variety of materials we have chosen for our mixtures are Mars-relevant phases, either previously detected on the Martian surface or plausibly present, based on what is known about Martian geochemical environments. In contrast to most terrestrial sediments, Mars sediments contain a significant fraction of primary igneous minerals (e.g., Morris et al., 2016; Rampe et al., 2017; Vaniman et al., 2013), so mixtures of hydrous and igneous minerals are clearly relevant for Mars.

Production of synthetic mixtures has a number of advantages. First, it allows us to systematically increase the proportion of hydrated material to investigate H peak increase in basaltic material, controlling precisely the relative change from sample to sample. Second, chemical matrix effects in LIBS data mean that line emission strength is sensitive not only to H content but can also vary due to the total elemental composition of the sample (e.g., Clegg et al., 2009), especially for H (Schroder et al., 2015, and references therein). At the same time, the limited set of chemical matrices and measurement conditions that ChemCam could encounter on Mars may help to reduce the complexity of their effects. Characterization of the H peak within basaltic matrices is thus most relevant for measurements of the Martian surface, which is mostly basaltic.

Mixture samples were produced from reagent grade chemicals or natural mineral samples that were already well characterized by chemical and mineralogical measurements (Table 1). All endmembers were mixed with K1919, a moderate-alkali (2.27 ± 0.01 wt.% Na_2O and 0.52 ± 0.01 wt.% K_2O) Hawaiian basalt chosen for its low hydration. In addition, for a subset of endmembers, mixtures were produced with GBW07105, a higher-alkali basalt (3.32 ± 0.01 wt.% Na_2O and 2.24 ± 0.01 wt.% K_2O) from the Brammer Standard Company. The other minerals chosen included a variety of salts, oxides, and phyllosilicates detected on Mars, some of which are hydrated or hydroxylated. The hydrated and hydroxylated minerals are expected to cause an increase in H line intensity with increasing concentration. The hydroxylated samples (e.g., brucite and epidote) are also important because their hydration is stable in spite of depressurization down to Martian pressures in a chamber. The nominally anhydrous materials (e.g., quartz and calcite) provide a check that H line intensity decreases with increasing concentration of anhydrous minerals in the mixture, thus allowing us to clearly define the limit of detection of the instrument.

The natural samples were first ground using a jaw crusher to produce submillimeter particles. All samples, both the reagent grade chemicals and the natural samples, were then run through a shatterbox for a few minutes to produce powders with grain sizes of $<250 \mu\text{m}$ for 85–90% of the particles (Anderson et al., 2017). This, importantly, is less than the spot size of the laser ($\geq 350 \mu\text{m}$). While some grain clumps or individual grains larger than the spot size of the laser existed within powders, we found no sporadic behavior in the shot-to-shot trends with depth that would indicate the laser sampling individual grains rather than a well-mixed powder. After preparation of the powders, we mixed the mineral samples at concentrations of 5, 10, 30, 50, and 70 wt.% with a basalt powder. Based on the shot-to-shot and spot-to-spot LIBS data collected from the mixtures, the powders were well mixed. Table 1 lists the set of mixtures we prepared. For some mixtures, we additionally prepared a mixture at 0.5 wt.% (where seven mixtures are listed in Table 1). Mixed samples were then pressed into pellets at 25 tons of pressure at room temperature.

2.1.2. Rock Samples

In addition to laboratory mixtures, we also measured a set of natural samples including previously characterized altered basalts from Iceland (Ehlmann et al., 2012) and altered basanites from San Carlos, AZ (Hadnott et al., 2017). LIBS measurements were taken of both powdered materials, which were pressed into pellets (prepared using the same methods as described in section 2.1.1) and small rock chips. The Iceland samples were formed in near-neutral pH, by surface and groundwater alteration of basalt lava flows (Ehlmann et al., 2012). The samples show a range of alteration, including filled veins and fractures. Samples from Hvalfjordur include hvalfj011 and hvalfj017, which sample friable rock at the contact between two lava flows; hvalfj025, which samples basaltic rock with celadonite- and silica-filled vesicles; hvalfj054, which samples zeolitized basaltic rock with filled vesicles; and icel009, which samples a massive basaltic outcrop. Both hvalfj011 and hvalfj054 have high-H zeolite inclusions that may have been included in the pelletized samples. The suite of alkaline basalts from San Carlos, AZ, exhibit different extents of alteration and represent weathering of alkaline basaltic rocks in an oxidative, semiarid environment (Hadnott et al., 2017). The samples vary from SanC-J, the least altered basalt with bright green olivine xenoliths, to SanC-A, a highly altered red-brown basalt with reddish olivine xenoliths. SanC-K is a relatively pristine basalt, SanC-F is a relatively

pristine basalt with a gypsum coating, SanC-B is intermediately altered, SanC-C is intermediately altered with red-brown xenoliths, and SanC-I is a highly altered red-brown basalt.

2.2. LIBS Measurements

LIBS spectra were collected using the Los Alamos National Laboratory (LANL) ChemCam-analog instrument described in detail by Clegg et al. (2017). The engineering model (EM) mast unit contains the laser, telescope, and remote micro imager (RMI). It is in an enclosure cooled to 4 °C and is connected by a fiber to the optical demultiplexer, spectrometers, and data processing unit in the body unit outside of the enclosure. The samples are placed into a vacuum chamber, which in less than 1 hr is evacuated and then filled with 7 ± 0.2 -mbar CO₂ to simulate Mars-like conditions at room temperature. Samples collected in 2013, 2015, and 2017 were measured at a laser-to-sample distance of 1.6 m while samples measured in 2014 were measured at 3.0 m. The distance difference was a result of the setup of the measurement system at the time and was not an intended experimental variable. Distance corrections were applied during data processing to account for the change in viewing geometry (Clegg et al., 2017; Wiens et al., 2013). The laser operates at 3 Hz with an energy of 14 mJ per pulse. The samples were measured with 50 consecutive laser pulses at each of five different locations across the surface to collect a total of 250 spectra per sample. Emission collected by the instrument's telescope was measured using three detectors across the following wavelength ranges: ultraviolet (UV; 240–340 nm), visible (VIS; 380–470 nm), and VNIR (490–850 nm).

We applied standard ChemCam ground data-processing techniques (Clegg et al., 2017; Wiens et al., 2013) to all LIBS spectra collected at LANL. This processing produces so-called clean, calibrated spectra files and includes the following correction steps: (1) subtraction of the background (measured spectrum with no laser pulse), (2) denoising, (3) continuum removal, (4) wavelength calibration, and (5) application of the instrument response function. The first five laser shots are excluded from analysis due to potential surface effects, the same standard number removed from ChemCam data from Mars. For analysis of H in the lab, removal of the first shots is especially important because the first shot has high H intensity due to a water surface layer (Kurniawan et al., 2014; Meslin et al., 2013). To minimize the influence of random single shot outlier variation, the median spectrum rather than the average spectrum was computed from the remaining 45 shots from each of the five spots, that is, utilizing 225 spectra.

2.3. Peak Fitting and Normalization of Spectra

The H peak height is not an accurate direct measure of the H emission because of interference from the adjacent C peak at 658 nm and broadening of the H emission line. For this reason, we fit the local 652- to 662-nm spectral region to measure the H emission using peak area. Figure 1 shows an example laboratory spectrum (both before and after continuum removal) including the local H region along with other spectral regions used for normalization. We use a Levenberg-Marquardt least squares minimization algorithm to fit two pseudo-Voigt peaks and a linear continuum. The approximate Voigt function, a fractional combination of a Gaussian profile (expected from pure Doppler broadening) and a Lorentzian profile (expected from collisional broadening), better fits the shape of the peaks than the Lorentzian function typically used. There are a total of nine free parameters in this peak fitting routine (linear continuum slope and intercept, peak height [2], full width at half maximum [FWHM; 2], center location [2], and the fraction Gaussian versus Lorentzian, which is assumed to be the same for both peaks), which is approximately 5 times less than the number of data points in the local H peak spectral region being fit. Additionally, Fe peaks are present in this region at 654.8 and 659.4 nm (Rapin et al., 2017a). We only fit these peaks with six additional parameters when necessary for the highest Fe-containing mixtures: the Fe sulfate and Fe oxide. We estimate the error in calculation of peak area by using the standard deviation of the peak area computed from the five separate spot measurements on a given sample.

We tested six methods for normalizing the hydrogen peak area to compensate for variability in the instrument (such as the laser energy and focus), experimental conditions (such as distance to the target and atmospheric pressure), and target properties (such as the physical and chemical matrix). By normalizing we mean dividing the hydrogen peak area by a proxy measured on the same spectrum, for instance the area of another peak. The first three normalization methods rely on using the peak areas of other elements assuming that they will reflect changes in the experimental parameters. The first method normalizes to the area of the C 658-nm peak (actually a mixture of two peaks—C II at 658.0 nm and C II at 658.5 nm forming

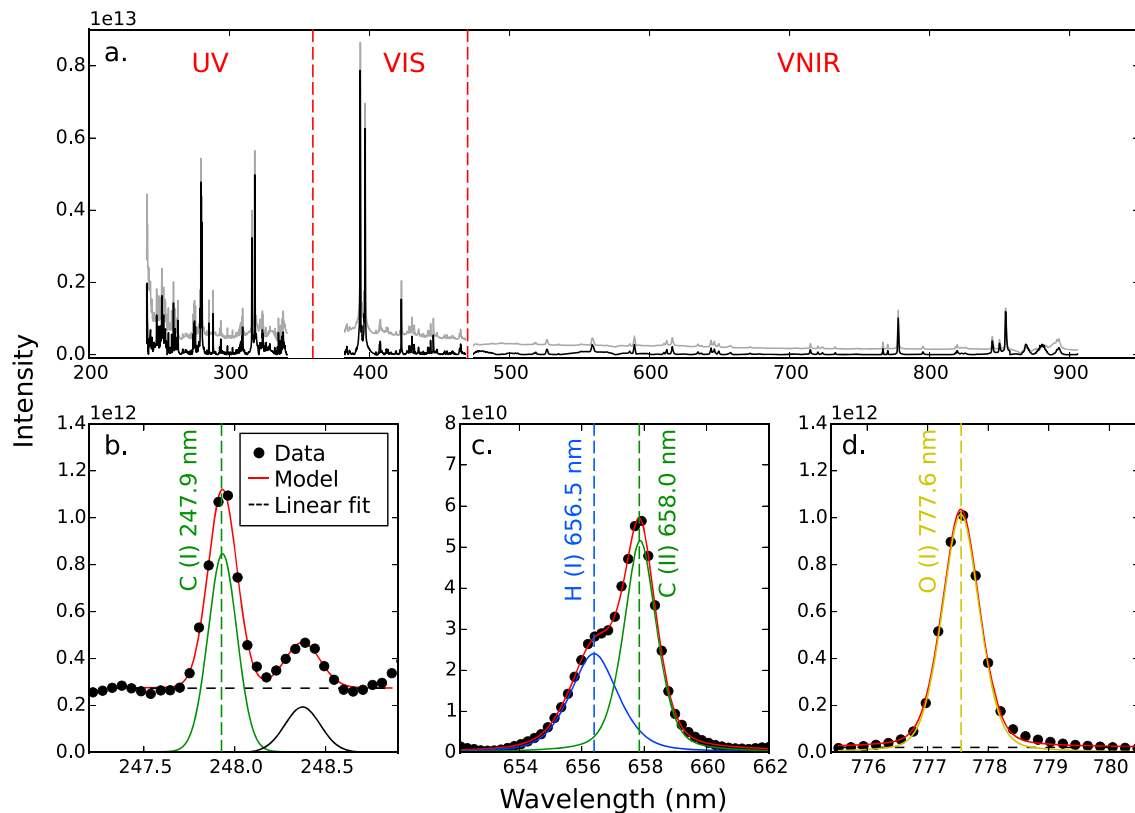


Figure 1. Spectrum of K1919 basalt and gypsum mixture at 50 wt.%. (a) Entire spectrum before (gray) and after (black) continuum removal across the three detectors (UV, VIS, and VNIR). (b) Example model fit to the data for the C (I) peak at 247.9 nm. The final model (shown in red) is a combination of a local linear continuum (black dashed line) and 2 Voigt peaks (green and black solid lines). (c) Spectrum of H-alpha (I) peak at 656.5 nm and C (II) peak at 658.0 nm. (d) Spectrum of O (I) peak at 777.6 nm. UV = ultraviolet; VIS = visible; VNIR = visible and near-infrared.

a single peak in ChemCam spectra as described by Schröder et al., 2018) from Martian atmospheric CO₂. This peak is fit simultaneously with the H peak at 656.5 nm, which is a neutral peak, in the initial analysis and could behave differently than the ionic C 658-nm peaks (Schröder et al., 2015). We also test normalization to the C I peak at 248 nm, fit separately from the H peak (also using a Voigt function), which is one of the normalization methods preferred by Rapin et al. (2016) and Rapin et al. (2017a). A potential complication of this method is that the C 248-nm peak is measured on a different detector than the H peak and detector behavior variability would not be corrected for. The third method normalizes to the oxygen peak at 778 nm, a triplet of neutral atomic emission peaks, which results from oxygen in atmospheric species and the target (Gasnault et al., 2012). The O peak area is also fit with a Voigt function. Another method tested is that previously used by Schröder et al. (2015), normalization to the continuum emission in the spectral region near the H peak, which results from Bremsstrahlung radiation and the broad tails of strong emission lines from other elements. This technique requires independent data processing, following all the processing steps normally required to generate the clean, calibrated spectra processed files except for continuum removal. Then, the continuum emission is estimated using the value of a nearby peak-free spectral region, here taken to be 660.0 nm. We also tested two standard ChemCam normalization methods called Norm 1 and Norm 3. Norm 1 normalizes the spectrum by the total spectral intensity across all detectors, and Norm 3 normalizes the spectrum by the spectral intensity of the VNIR detector only, which is the detector for the H-alpha line, both after continuum subtraction. These two techniques depend on the emission lines and, therefore, elements present in the sample, so can be impacted by variations in composition.

2.4. Independent Characterization

Additional powders of the same sample endmembers and a subset of the mixtures (10 and 50 wt.% samples) were independently characterized by Activation Laboratories Ltd. (Actlabs) using flux-fusion inductively coupled plasma optical emission spectroscopy for the major oxides, instrumental neutron activation

Table 2
Thermogravimetric Analysis Results

Sample	Loss below 150 °C (wt.%)	Loss below 400 °C (wt.%)	Loss below 900 °C (wt.%)	H ₂ O (wt.%)	H (wt.%)
Ca chloride	4.82	29.76	30.75	30.75	3.44
Na chloride	0	0	4.08	0	0
Ca carbonate	0.02	0.08	43.48	0.08	0.01
Mg carbonate	0.59	0.89	53.29	0.89	0.10
Alunite	1.24	2.74	9.67	7.94	0.89
Gypsum	2.97	20.71	20.9	20.9	2.34
Fe sulfate	8.09	27.17	69.64	27.46	3.07
Mg sulfate	2.19	15.65	16.58	16.79	1.88
Na sulfate	0	0	0.09	0	0
NAu-1	6.26	9.92	14.86	14.86	1.66
NAu-2	6.98	9.46	13.55	13.55	1.52
Quartz	0	0	0	0	0
Opal 1	0.98	2.33	3.83	3.83	0.43
Opal 2	0.7	2.04	3.6	3.6	0.40
Opal avg.	0.84	2.18	3.72	3.72	0.42
Brucite	0.33	3.49	30.88	30.88	3.46
Epidote	0.11	0.36	0.61	0.76	0.09
Hematite	0.08	0.51	0.6	0.6	0.07
Muscovite	0.44	1.2	4.14	5.26	0.59
Serpentine	1.27	2.58	10.28	10.28	1.15
hvalfj011 1	1.72	2.75	3.41	3.48	0.39
hvalfj011 2	1.52	2.54	3.18	3.28	0.37
hvalfj011 avg.	1.62	2.64	3.3	3.38	0.38
hvalfj017	4.89	7.67	9.55	9.55	1.07
hvalfj025 1	0.41	0.56	0.46	0.71	0.08
hvalfj025 2	0.57	1.01	0.83	1.22	0.14
hvalfj025 avg.	0.49	0.78	0.64	0.97	0.11
hvalfj054 1	2.57	5.93	7.22	7.23	0.81
hvalfj054 2	1.87	5.2	6.14	6.14	0.69
hvalfj054 avg.	2.22	5.57	6.68	6.69	0.75
icel009 1	0.54	0.75	0.86	1.01	0.11
icel009 2	1.52	2.52	2.89	2.96	0.33
icel009 avg.	1.03	1.64	1.88	1.98	0.22
K1919 1	0.03	0.11	0.12	0.12	0.01
K1919 2	0.02	0.11	0.12	0.12	0.01
K1919 avg.	0.02	0.11	0.12	0.12	0.01
GBW07105 1	0.83	2.94	3.3	3.5	0.39
GBW07105 2	0.82	2.94	3.29	3.49	0.39
GBW07105 3	0.84	2.98	3.32	3.53	0.40
GBW07105 4	0.7	2.84	3.19	3.4	0.38
GBW07105 avg.	0.8	2.93	3.27	3.48	0.39

Note. Cumulative weight percent lost in the <150, <400, and <900 °C temperature ranges. Error in thermogravimetric analysis measurements is ±0.015 wt.%. See text (section 2.4) for details of the computation of H₂O weight percent for each phase. H weight percent is computed from stoichiometry from H₂O weight percent.

analysis for Cl, and infrared spectroscopy for C and S to verify the endmember composition and the accurate production of the mixtures.

The H (or H₂O) content of a given mineral must be measured and cannot be determined from stoichiometry because samples can contain adsorbed and structural H₂O or OH such that even nominally anhydrous minerals often contain measurable amounts of hydrogen. The amount of H₂O incorporated depends on both pressure and temperature, which makes determining hydration challenging, particularly under different environmental conditions. TGA was used to independently characterize the hydrogen content of all samples by measuring the weight percent H₂O released upon heating. The release temperature of water serves as a proxy for how easy or difficult samples are to dehydrate upon exposure to low pressures, as in the Mars chamber used for LIBS measurements. TGA measurements were performed using a Perkin-Elmer STA 6000 instrument. Samples were heated in air to 900 °C at a rate of 10 °C/min while monitoring weight change. Samples were then held at 900 °C for 1 hr to ensure all H₂O was removed, again, while monitoring weight change.

We estimated the total weight percent H₂O for each of our samples by calculating the weight percent lost over the temperatures where water is removed as described by Földvári (2011). First, adsorbed and nonstructural H₂O are removed at temperatures typically below 150 °C as evidenced by the weight percent loss of our samples below 150 °C (first column of Table 2), a temperature chosen as a reference similar to previous studies (e.g., Földvári, 2011; Vaniman & Chipera, 2006). At higher temperatures, generally near 500 °C, structural H₂O is lost. Besides the exceptions listed next, we calculated the total H₂O content of our samples using the sample's total weight lost over the entire TGA temperature range plus the additional 1 hr of heating at 900 °C. The exceptions to this are (1) SO₄ is released from the Fe sulfate, Na sulfate, and alunite samples at temperatures above 600 °C, so weight percent H₂O for these minerals was calculated using temperatures below 600 °C. (2) Weight percent H₂O for NaCl was calculated from the weight lost below 150 °C because halite does not hydrate under nonzero humidity and should only have small amounts of adsorbed water present. Any weight percent change above 150 °C is due to melting (at 800 °C) and evaporation of the sample. On the other hand, our Ca chloride sample is nominally anhydrous but readily hydrates under nonzero humidity, so the entire temperature range is used. (3) For the nominally anhydrous carbonate minerals, the high temperature weight loss is due to CO₂ being burned from the sample, so weight percent H₂O was calculated using loss below 400 °C. (4) For some of the basalt samples, the minimum weight often did not occur at the highest temperature reached (900 °C). Instead, the basalt samples sometimes reached a weight percent minimum at slightly lower temperatures. This difference (<0.5 wt.%) is likely a minor calibration issue with the

instrument at highest temperatures rather than a real weight percent gain at high temperatures. Therefore, we calculated the weight percent H₂O for the basalt samples using the minimum value of the TGA curve.

We estimated the precision of the TGA measurements by repeat measurements of a few endmembers (the K1919, GBW07105, hvalfj011, hvalfj054, and icel009 basalts and the opal sample). While most of the samples are very consistent across runs with repeat measurements having standard deviations of 0.05–0.26 wt.%, two of the natural basalt samples (icel009 and hvalfj054) showed variation of ~1 wt.%, perhaps indicating aliquot

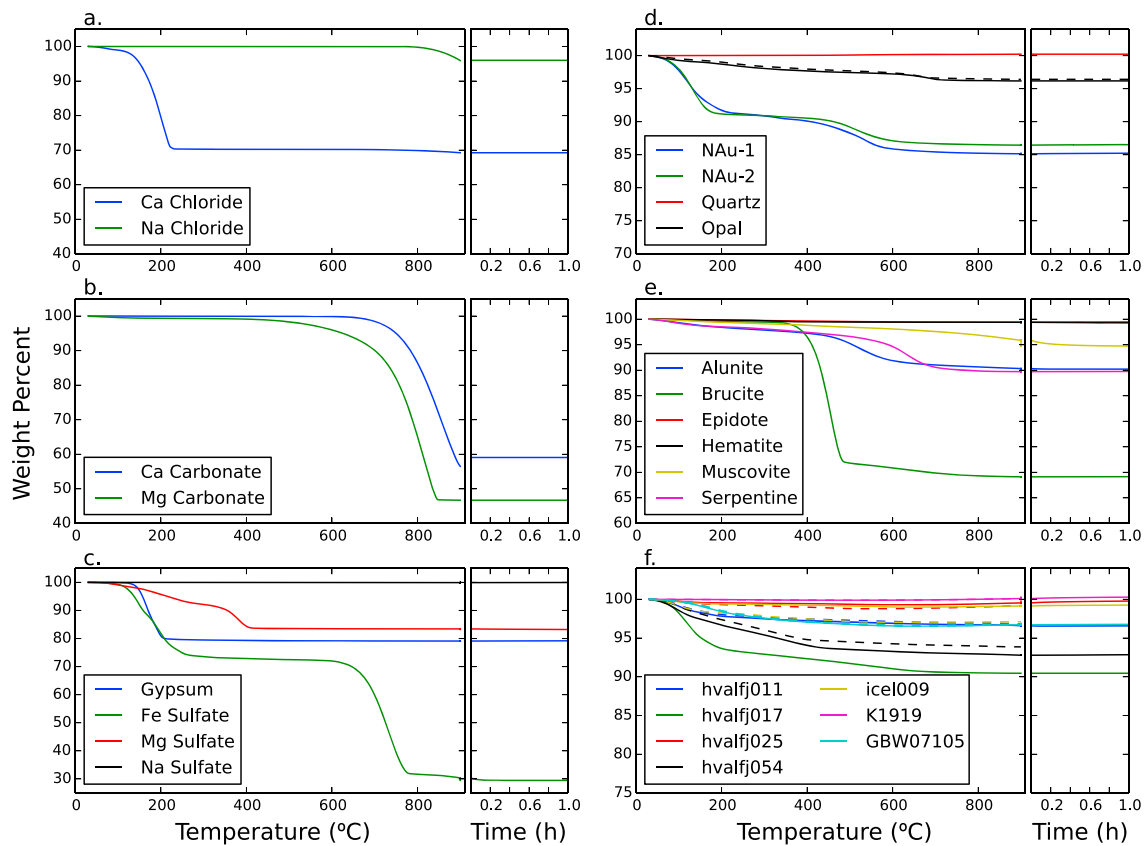


Figure 2. Thermogravimetric analysis for (a) chlorides; (b) carbonates; (c) sulfates; (d) silica, hydrated silica, and nontronite standards; (e) hematite and minerals, which, based on stoichiometry, are only hydroxylated; and (f) basalts and rock samples.

variation for these samples. Ultimately, the accuracy of the TGA measurements for use in determining H content is limited by potential water loss during pump down to vacuum (see section 3.2).

2.5. ChemCam Data

ChemCam spectra are collected by Curiosity using a very similar LIBS instrument to the LANL analog instrument used for our study. Typical ChemCam observations on a given point collect 30 shots at 3 Hz. When we average laser pulse spectra obtained at a single observation point, the first five shots are ignored due to potential contributions from surface materials like dust or thin coatings. We fit the ChemCam spectra using the same procedures as the laboratory data with an additional constraint on the FWHM of 0.9 nm, a physically reasonable upper limit determined based on the largest H FWHM observed in the laboratory data. We also apply the Earth-to-Mars correction as described by Clegg et al. (2017) to account for differences in sensitivity between the LANL laboratory and ChemCam instruments. Targets are generally 2.2 to 7 m from the instrument with most at about 3 m (Maurice et al., 2016). ChemCam collects images of the targets in complement to the LIBS spectra using the RMI. We have visually classified individual ChemCam points using the RMI images up to sol 1815 in order to identify where veins have been targeted for comparison with the results of Rapin et al. (2016; 69 points) and where ChemCam has shot smooth bedrock (2,098 points) for calculation of its H content.

3. Results

3.1. Thermogravimetric Analysis

TGA analysis shows our samples contain between 0 and 31 wt.% H₂O or 0 and 3.5 wt.% H (Figure 2; Table 2). The minerals with structural H in metal-OH bonds lost H₂O at high temperatures (≥ 400 °C). Other minerals lost weight at stepped temperatures. CaCl₂ tends to be hygroscopic and shows dehydration at 200 °C. In contrast,

NaCl lost weight only through melting and evaporation of Cl (Figure 2a). The carbonate minerals (Figure 2b) we measured lost CO₂ at high temperature (>700 °C) in the general reaction $XCO_3 \rightarrow XO + CO_2$. Additionally, a small amount of adsorbed or loosely bound water was released at low temperatures (<200 °C) from the Mg carbonate (Figure 2b). While nominally anhydrous, the Mg and Fe sulfates hydrate readily under nonzero humidity. For these and for gypsum, dehydration occurs at temperatures well below 400 °C while SO₃ is released above 650 °C (Figure 2c). Figure 2d shows TGA results for a variety of Mars-relevant silicates and oxides, some of which are hydrated. For the nontronite samples, NAu-1 and NAu-2, endothermic dehydration occurs between 100 and 200 °C and dehydroxylation occurs between 400 and 500 °C (Ding & Frost, 2002; Földvári, 2011). Opal was measured twice using TGA, and the weight percent loss trends are very similar between samples. Opal dehydrates by losing H₂O from its structure continuously up to approximately 700 °C. As expected, the quartz sample is not hydrated and does not lose any appreciable weight in the 100–900 °C range. Most hydroxylated materials did not dehydrate until 400 °C, although alunite and serpentine show evidence for continual slow dehydration over the temperature range, suggesting some H₂O or impurities (Figure 2e). Hematite, as expected, had no loss. Finally, the basaltic endmembers used in this experiment (K1919, 0.1 wt.% H₂O; GBW07105, 3.5 wt.% H₂O) and natural samples from Iceland measured with TGA show loss over a wider range of temperatures (from the start of heating to 700 °C; Figure 2f). The most altered and smectite-rich sample (79 wt.% smectite), hvalfj017, has the highest weight percent loss. Loss for the Iceland natural samples was assumed to be in the form of H₂O as other volatile-bearing minerals were not detected in X-ray diffraction (Ehlmann et al., 2012).

3.2. LIBS H Peak Versus H Content

The C peak at 658 nm due to the CO₂ atmosphere in the sample chamber is clearly visible in all mixtures near the H peak (Figure 3). The laboratory mixtures that show an increasing H peak with weight percent endmember are gypsum (mixed with both K1919 and GBW07105 basalts), Ca chloride, Mg sulfate, alunite, Fe (III) sulfate, opal, NAu-1, NAu-2, brucite, muscovite, serpentine, Mg carbonate, and epidote. No appreciable change is observed for Na chloride, Ca carbonate, quartz, hematite, and Na sulfate. In some cases, decreasing H was observed with increasing weight percent endmember in question. For example, the NaCl with GBW07105 mixture shows decreasing H because the basalt is more hydrated than halite. Adjacent to the H peak in the 100 wt. % hematite sample, there is a strong emission line at ~655 nm. This Fe emission line is only observed in the highest FeO weight percent samples of the basalt-hematite and basalt-Fe-sulfate mixtures. This peak is fit for the hematite and Fe sulfate mixtures but may not be fully accounted for in the case of Fe sulfate (Figure 4).

We used the methods described in section 2.2 to peak-fit all the mixtures that showed increasing H emission with weight percent endmember. Then, we compared peak area H with weight percent H determined using TGA. H peak area (or signal) increases with H weight percent for all the mixtures, though the curve shape and slope differ by mixture (Figure 4). We fit three different trend lines to the observed signal by minimizing the modified χ^2 calculated using the equation: $\chi^2 = \frac{(y-M)^2}{\sigma_y^2 + \sigma_x^2 \left(\frac{dy}{dx}\right)^2}$, where M is the model value and σ_x and σ_y are the errors on x (weight percent H) and y (LIBS H signal), respectively. The modified χ^2 allows us to take into account error both in our fit LIBS signal (described in section 2.3) as well as error in our TGA measured weight percent H values. The error in weight percent H due to the precision of our TGA measurements is relatively small as we discuss in section 2.4, but the error due to accuracy is larger. One effect that may influence the trends shown in Figure 4 and cause scatter in the data is loss of water after placement in the chamber for measurement. Because our samples are pumped down to vacuum and then set to 7-mbar CO₂, our samples almost certainly lost H₂O before LIBS measurement during pump down. We take the weight percent loss below 150 °C as a proxy for the potential amount of adsorbed or loosely bound water lost in the vacuum chamber during the LIBS measurement process (Milliken & Mustard, 2005; Vaniman & Chipera, 2006). We use this quantity, column 2 of Table 2, as σ_x , the accuracy in our TGA measurements.

H peak area increases versus weight percent for all six normalizations (Figure 4). Examination of the best linear fit to all mixtures and basalt samples (black dashed line; Figure 4) shows that above 1.25 wt.% H, the increase in LIBS H signal is not clearly linear, particularly for the C 658- and O 778-nm normalizations. We also fit a second-order polynomial function ($ax^2 + bx + c$) to the data (shown in magenta) to describe this increase. Mixtures containing less than ~1.25 wt.% H mostly follow a linear relationship, so we also show a separate

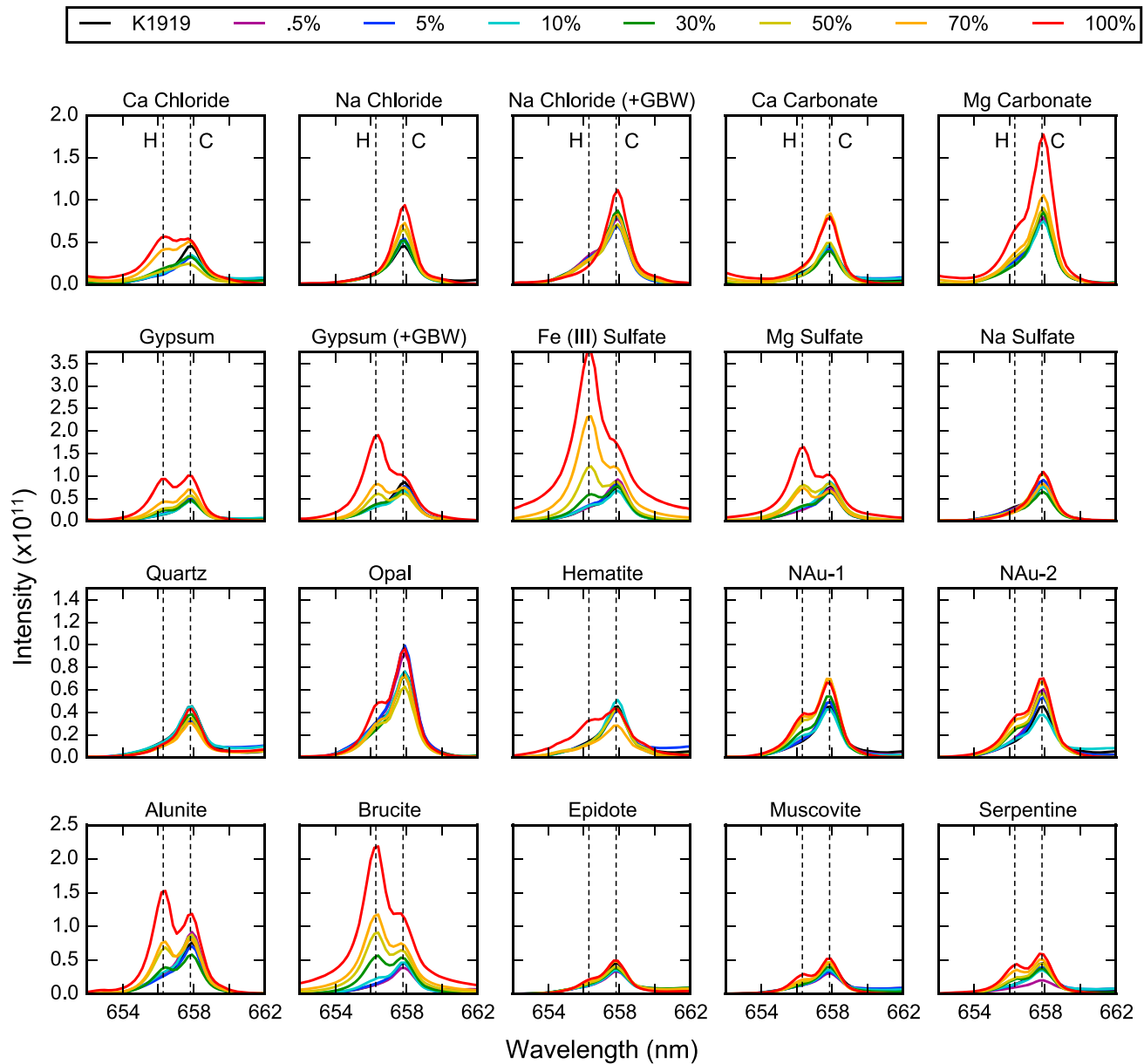


Figure 3. Laser-induced breakdown spectroscopy spectra of all laboratory mixtures showing the local H peak region from 652 to 662 nm including the H (I) peak at 656.5 nm and the C (II) peak at 658 nm. Colors indicate weight percent of listed endmember from 0% for pure basalt (black) to 100% pure mineral endmember (red).

linear fit to all measurements below 1.25 wt.% H (shown in turquoise). The coefficients for all the fit trend lines are included in Table A1. Alunite has a clearly distinctive trend, diverging from the linear fits even at low weight percent H. The sulfates like Fe and Mg sulfate tend to fall above the fit trend line even for some lower weight percent H mixtures. For Fe sulfate the higher H peak area than expected from the TGA results is likely due to interference from the Fe peaks adjacent to the fitted H peak, as evidenced by a small shift in the H peak center location. Observed differences between sample suites in the normalized area versus weight percent H are similar across normalizations.

To test the goodness of fit to the three models (linear, low weight percent linear, and second-order polynomial), we calculated the root-mean-square error (RMSE) of cross-validation (RMSECV), which leaves out one data point to estimate how well the model built on the rest of the data set performs for unknown cases. We used the equation

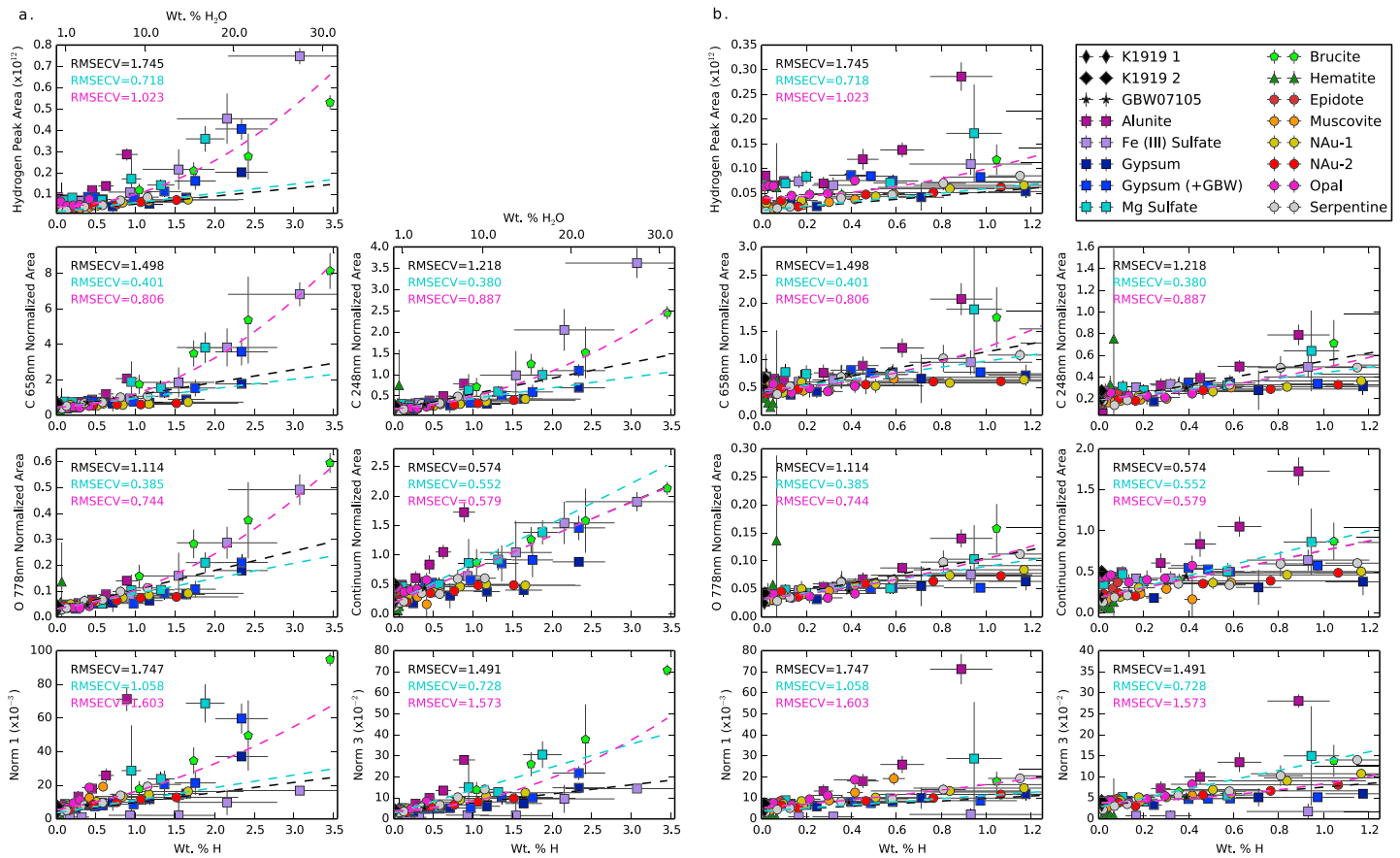


Figure 4. Hydrogen emission peak area versus weight percent hydrogen for full temperature range for all samples, as reported in Table 2, for the (a) full weight percent range and (b) the low weight percent range. The black dashed line is a linear fit to all the samples; the turquoise line is a linear fit to samples with H wt.% < 1.25%; and the magenta is a second-order polynomial fit to all samples. RMSECV values (calculation described in section 3.2) are included for comparison between normalizations. Error bars are computed using methods described in section 2.2. For the continuum normalization, the best linear fit (black) and polynomial fit (magenta) trend lines overlap. Trend line coefficients are included in Table A1. RMSECV = root-mean-square error cross-validation.

$$RMSECV = \sqrt{\frac{\sum_{i=1}^n (y_i - \hat{y}_i)^2}{n}}, \quad (1)$$

where y is the measured values of LIBS H signal, \hat{y} is the LIBS H signal estimated by cross-validation (where the value for each object i is estimated using a model that was built using a set of objects that does not include object i), and n is the total number of data points. RMSECV values were normalized by the median value of the data set because the LIBS H values differ by orders of magnitude across the different normalizations. Normalization to O 778 nm, C 248 nm, and the continuum visually produce the least scatter in the data and produce the lowest RMSECV values for the full-range linear model (Figure 4). Nonetheless, the fits clearly show that the relationship between peak area and weight percent H₂O is not linear for the full sample suite over the 0–3.5 wt.% H range examined. The polynomial model performs better for the higher weight percent H samples and produces low RMSECV values for norm1 and norm3. Calculation of the x axis as mole percent H instead of weight percent H does not affect this finding (Figure A2).

Scatter is introduced into our measurements due to loss of H₂O before LIBS measurement in the vacuum chamber. Consequently, we next consider only a subset of the mixtures that have structurally bound H (brucite, epidote, muscovite, nontronite, and serpentine; Figure 5). These samples also released some H at low temperatures in our TGA experiments, so we compare LIBS H peak area with the weight percent H calculated from weight loss above 150 °C because nonstructural H₂O should be lost by this temperature (Milliken & Mustard, 2005; Vaniman & Chipera, 2006), although we still consider our x axis error bars as the TGA weight percent lost below 150 °C. For all normalizations, LIBS H emission increases monotonically

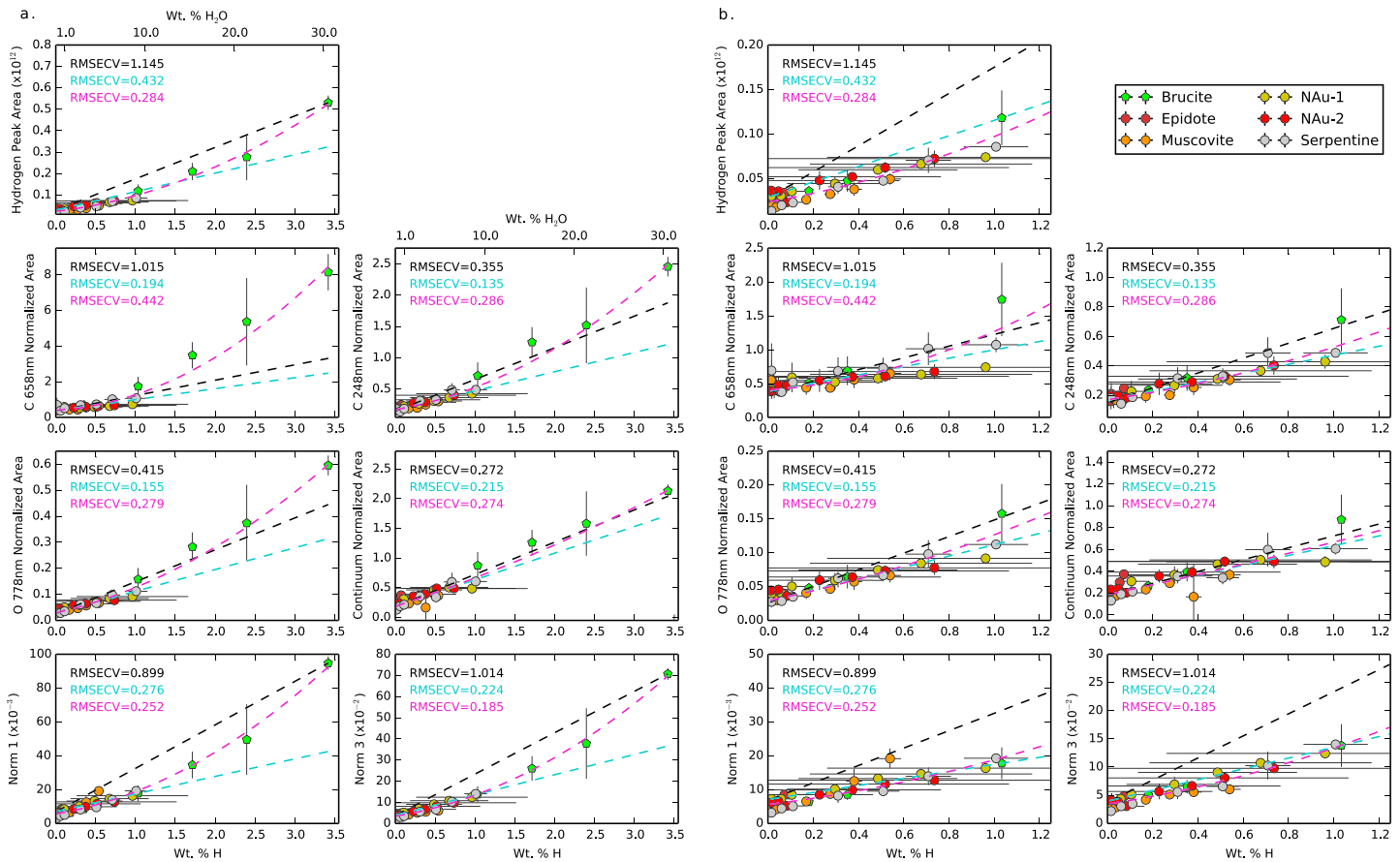


Figure 5. Hydrogen emission peak area versus weight percent hydrogen, for the full weight percent range (a) and low weight percent range (b), when calculated only from water temperatures $>150^{\circ}\text{C}$, for a subset of the sample data from Figure 4, including only those samples that have bound OH. The black dashed line is a linear fit to all the samples; the turquoise line is a linear fit to samples with H wt.% $< 1.25\%$; and the magenta is a second-order polynomial fit to all samples. Trend line coefficients are included in Table A1. RMSECV = root-mean-square error cross-validation.

with weight percent H. Scatter from the linear trend lines for these fits (Table A1) is considerably lower than for the full sample set for all normalizations (Figures 4 and 5). However, the trend still significantly steepens for high H contents, wt.% H $> 1.25\%$, in the brucite mixture.

We quantify the uncertainty in our ability to predict weight percent H from the LIBS H signal by measuring the scatter from our fit linear trends. The RMSE for the fit lines for the O 778 nm and C 248 nm normalizations for the Figure 5 samples are, respectively, ± 0.42 and ± 0.43 wt.% H for the full linear fit, ± 0.24 and ± 0.18 wt.% H for the linear fit of samples with < 1.25 wt.% H, and ± 0.31 and ± 0.30 wt.% H for the polynomial fit.

Our ability to detect the LIBS H signal is limited by interference due to the adjacent C peak and Fe peak. We can use our lowest weight percent H samples where H emission is observed to estimate the detection limit as done by Rapin et al. (2017a). Samples with weight percent H over ~ 0.9 wt.% H₂O visually exhibit an inflection at 656.5 nm such as the Mg carbonate and epidote endmembers (Figure A1). In some instances, an asymmetry of the C 658-nm peak is observed, which may be indicative of H at even lower abundances, for example, Ca carbonate. Samples with approximately 0 wt.% H₂O like Na chloride exhibit the smallest amount of asymmetry in the C 658-nm peak. We can also calculate the detection limit using the standard equation $LOD = 2sm$, where s is the standard deviation of the measurements for our lowest concentration samples and m is the slope of the fit trend line. Using our low concentration calibration curves in Figure 5, we find a detection limit of 0.10 wt.% H for the C 248-nm normalization and 0.04 wt.% H for the O 778-nm normalization. This equates to 0.4–0.9 wt.% H₂O, which is similar to value where the peak visually becomes apparent as described above.



Figure 6. Variation in H, C (II) 658-nm, C (I) 656-nm, and O (I) 778-nm peak areas and continuum emission nearby H (660 nm) with shot number for a low-moderate weight percent H mixture (NAu-2) and a high weight percent H mixture (brucite). Each 50 shots is a different location on the sample and colors indicate increasing weight percent NAu-2 or brucite.

3.3. Shot-To-Shot Behavior

The peak intensity of H typically decreases with increasing laser shots (Figure 6; as also seen by Rapin et al., 2017a). After the first shot with high H, there is a systematic, slow decrease in intensity with shot number. The 50, 70, and 100 wt.% brucite mixtures are exceptions and show relatively constant, high H intensity across all shot numbers (Figure 6b).

We expect the lab chamber to remain at constant $p\text{CO}_2$, but because laser-target coupling can vary with target texture and composition, C and O emission may not necessarily remain constant. Empirically, we have found that emission of the C peak at 658 nm, the C peak at 248 nm, and the O peak at 778 nm all decrease steadily with shot number like H (Figure 6; Figure A3). In contrast, the continuum level adjacent to the H peak increases with shot number across all sample locations. Nevertheless, division by any of these still results in monotonic H peak area increase with weight percent H (Figures 4 and 5).

The range of shot numbers used to calculate the LIBS H signal impacts the calibration curves across all normalizations (Figure 7). The signal decreases with increasing shot number leading to lower slopes with shot number for the mixture sets shown: gypsum and muscovite. Similarly, most major element lines like Si show decreasing intensity with shot number although Ca lines in the gypsum mixture increase in intensity with shot number (Figure 8).

3.4. LIBS H Line in Natural Samples

H peaks are not prominent for the powdered and pelletized San Carlos and Iceland samples but, generally, asymmetry of the C emission line indicates a hydrogen contribution from aqueous alteration that is

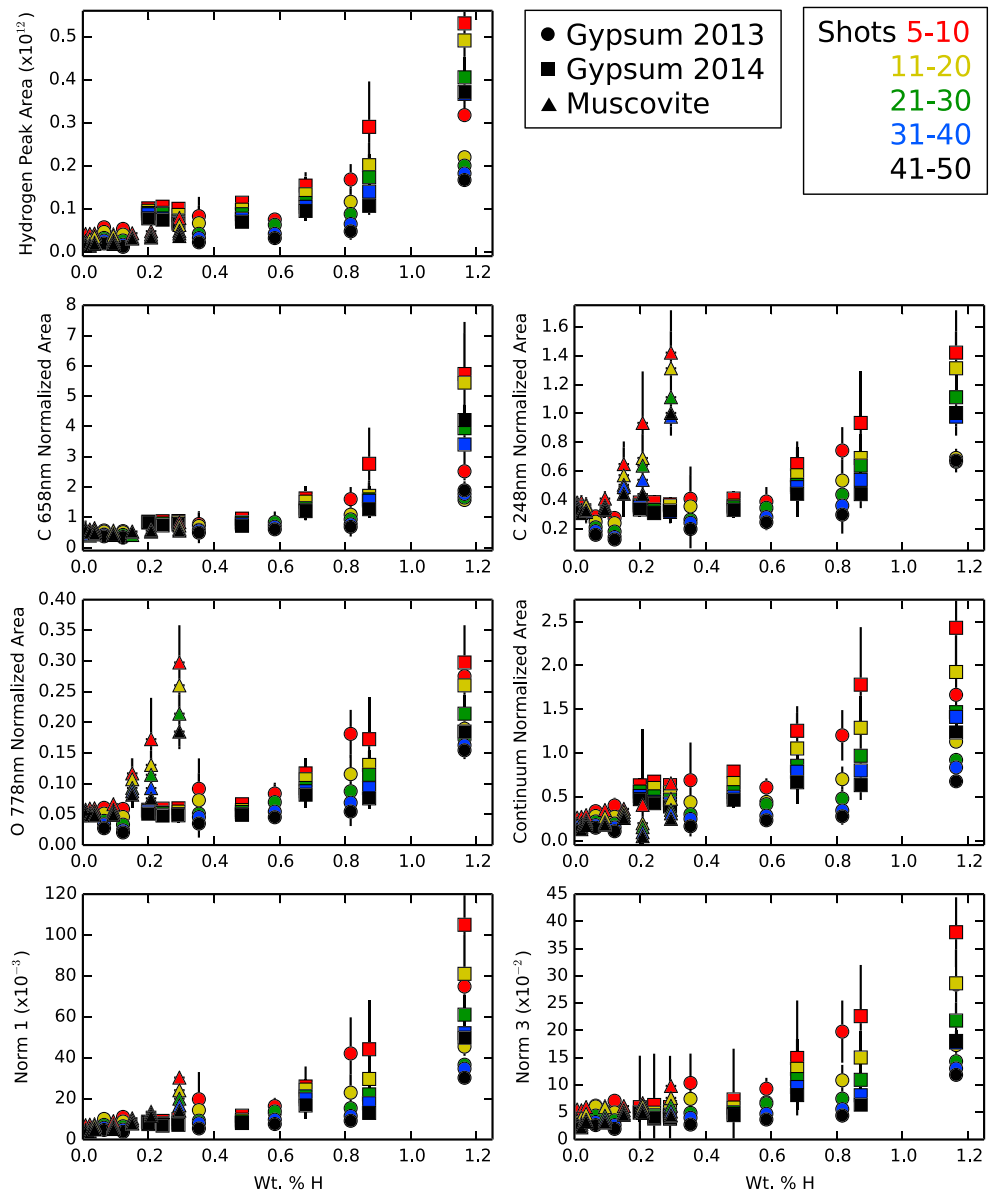


Figure 7. Variation in the increase in laser-induced breakdown spectroscopy H signal versus weight percent H for different ranges in shot number: 5–10 (red), 11–20 (yellow), 21–30 (green), 31–40 (blue), and 41–50 (black). Under all normalizations, the H signal decreases with increasing shot number.

highest for the most-altered samples (Figure 9). Among the San Carlos samples, the least altered (SanC-J) shows only a broad shoulder to the C peak at 658 nm indicative of low H whereas even minimally altered samples like SanC-B (<10% clay mineral) show an H peak (Figure 9a). The sedimentary sample, SanC-S, has the highest H peak. In the Iceland samples (Figure 9b), the existence of the H peak suggests hydration/hydroxylation of the basaltic rock. The samples hvalfj054 and hvalfj017 have the highest H peak, consistent with their having the highest hydrous mineral content (Ehlmann et al., 2012), though the difference with other samples is small.

Interestingly, all the corresponding rock chips from the Iceland natural samples show a change in H peak shape relative to the powdered pellets, and the H emission peak is typically higher for the rock chip spectra than for the powdered pellet spectrum. As expected, some rock chips show more variation in H peak area across the different spots on the target, for example, hvalfj054, which has zeolite-filled vesicles (larger than the spot size of the laser spot size; Figure 10).

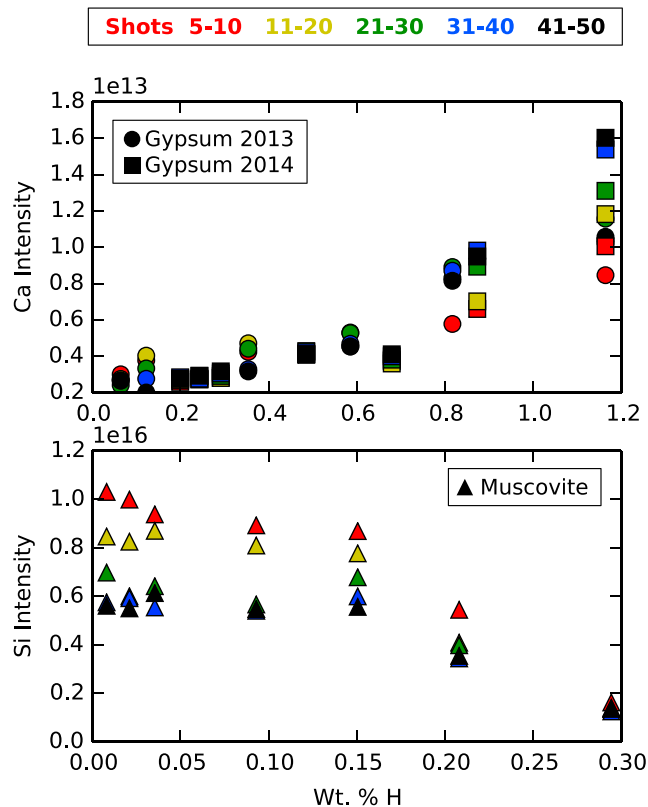


Figure 8. Top: Ca emission line (318.025 nm) variation with shot number in gypsum mixture. Bottom: Si emission line (188.242 nm) trends with depth for muscovite mixture. Ca increases and Si decreases with increasing shot number: 5–10 (red), 11–20 (yellow), 21–30 (green), 31–40 (blue), and 41–50 (black).

Normalized H line area versus weight percent H (lost above 150 °C) was also calculated for the natural rock chips and powders and compared to the linear fit from Figure 5 (Figure 11). Because these natural samples contain smectite clays, mixtures of the nontronite samples (NAu-1 and NAu-2) and basalt are also shown for comparison. The rock chip samples do not fall on a linear trend and show large scatter, but the pelletized samples generally follow the nontronite samples in the normalized data. Both basalts measured in the second batch of samples, GBW07105 and K1919, do not fall near the linear fit (see section 4.1 for discussion). The O 778-nm, C 248-nm, and continuum normalizations provide the best match between the natural samples and H linear fit calibration lines.

3.5. Use of Calibrations to Determine H in ChemCam Spectra From Mars

We examine the sensitivity of interpretations of ChemCam LIBS spectra to the different calibration approaches. One example important to interpreting Mars data is measurement of the hydration state of various salts, which have been reported based on orbital data and found in situ by rover missions. We use the Figure 5 calibration lines (Table A1) for each of the normalizations from our work to predict the H peak values for bassanite ($\text{CaSO}_4 \cdot 0.5 \text{H}_2\text{O}$) and gypsum ($\text{CaSO}_4 \cdot 2 \text{H}_2\text{O}$) on Mars and then compare these to the H signal observed for veins up to sol 1248 (same sample set examined by Rapin et al., 2016). Under all normalizations, the distribution of the ChemCam LIBS data normalized is closer to bassanite and would more likely be predicted to be this mineral using all of the normalizations. In particular, normalization to C 248 nm, O 778 nm, and Norm 3 all agree well on bassanite composition. The normalized H signal predicted for gypsum falls outside of the observed ChemCam vein distribution for all calibration approaches except C 658 nm and Norm 1, and for these calibrations the mean of the measured distribution falls between bassanite and gypsum.

We also use our data to examine the water content of Martian rocks, specifically the Murray formation, a fine-grained, thinly laminated mudstone facies, which is the lowermost strata of the Mount Sharp group. We analyzed the RMI images by eye to exclude rough targets, those where ChemCam shot loose sediment (sand and dust), and diagenetic features that may have a different H signal. We also exclude points with bad focus and low major-element totals (<87%). In total, we included 229 ChemCam targets in our analysis from sols 766–1815. Using the C 248-nm normalization, the range in H content for the middle 50% of the data is 2.0–4.1 wt.% H_2O with a median of 3.0 wt.% H_2O . The O 778-nm normalization predicts a median value of 2.3 wt.% H_2O with the middle 50% ranging from 1.3 to 3.3 wt.% H_2O . These values are consistent with the total oxide percentages derived from ChemCam, which have a median of 97.0 wt.% for the bedrock points we considered. When we take the weight percent H_2O calculated from our calibrations and add it to the ChemCam derived total oxide percentage, we get a median total of 99.6 wt.% for the O 778-nm calibration and 100.2 wt.% for the C 248-nm calibration. Some low water content samples (8 with the C 248-nm normalization and 17 with the O 778-nm normalization) plot with less than 0 wt.% H_2O because our laboratory calibration did not require the y intercept to be 0. A small number of high outliers include individual points predicting up to 25% H_2O , which may target high H compositions.

4. Discussion

4.1. Normalized H Peak Area Calibration Curves

The use of H calibration standards that do not lose water under vacuum was key in our study (see Figure 4 versus Figure 5). By using our TGA measurements to correct the weight percent H to account for the loss of nonstructural H_2O in the vacuum chamber before LIBS measurement, we correct for some of the scatter due to uncertainty in sample water retention. This highlights the importance of stability of

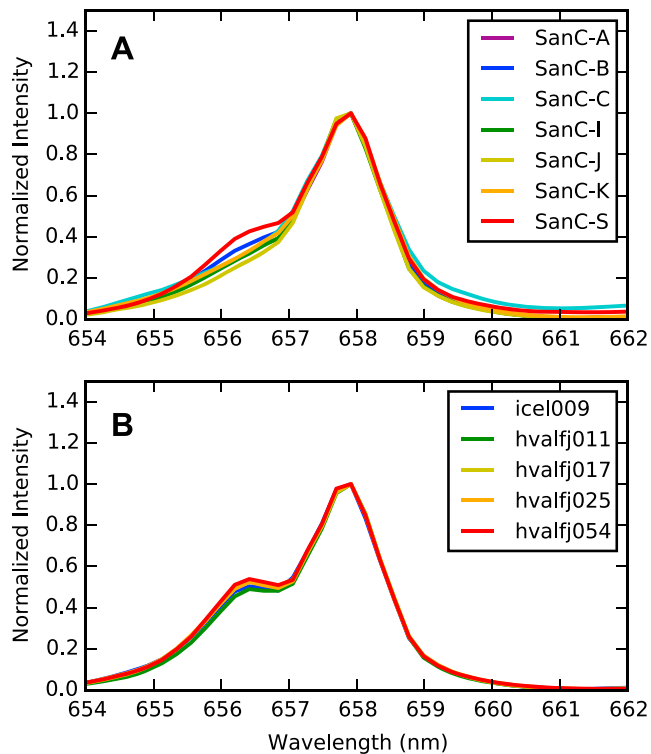


Figure 9. Laser-induced breakdown spectroscopy spectra normalized to the height of the C peak at 658 nm of all pressed pellet natural rock samples measured from San Carlos (a) and Iceland (b).

H for future investigators of H emission line calibration. Future studies might consider producing glasses of controlled OH contents or including a balance within the vacuum chamber to monitor the sample directly.

All normalizations show similar behavior—a monotonic increase of H peak area with increasing sample H weight percent—and perform better than nonnormalized H peak area, evaluated by computed RMSECV (Figure 5). The continuum, C 248-nm, and O 778-nm normalizations produce the lowest RMSECV values for the three fit trends (Figures 5), similar to the results of Rapin et al. (2017a) who preferred C 248 nm. C 658 nm also has scatter that is nearly as low but is likely complicated by the interference from the H peak of interest, while whole spectra norm1 and norm3 may be affected by variation in sample composition causing variation in line area unrelated to anything affecting or proportional to the H signal.

We favor normalization to C 248 nm and O 778 nm due to the shot profile behavior of these peaks. As discussed in section 3.3, these individual peaks decrease in intensity with shot number like the H peak. The continuum intensity and single or total detector intensity (Anderson et al., 2017) increase with shot number or are simply variable, which can increase variation of the hydrogen signal after normalization (as also shown by Rapin et al., 2017a). While the O 778-nm peak is caused both by breakdown of atmospheric CO₂ and the sample bulk O content, O 778-nm normalization is not greatly biased by changes in the sample O content because the majority of variation in the O 778-nm peak is due to variations in the measurement conditions such the atmospheric constituents and pressure (Gasnault et al., 2012). In addition, O 778 nm is

another neutral emission line with similar excitation energy to H (H Ek = 10.2 eV; O Ek = 10.7 eV). The similar excitation energies could make this normalization less sensitive to matrix effects (Lazic & De Nino, 2017). For this reason and from the experimental results in Figure 12 with samples acquired under different experimental conditions, the O 778-nm normalization may be the simplest to produce quality results.

Normalization to C 248 nm was slightly favored in the results of Rapin et al. (2017a). One reason for the slight difference from this study may result from the three different instruments located on Mars, in Toulouse, and at LANL. The latter instrument was used for this study, and it consists of an EM mast unit with a newly built body unit. Rapin et al. (2016) and Rapin et al. (2017a) used the Toulouse instrument for their laboratory studies, and it consists of an engineering qualification model (EQM) mast unit and an EM body unit. A change to the mast unit that was made between the EM and the EQM affects the quality of the lower portion of the UV spectral range, where the C 248-nm line resides. Specifically, the LANL EM mast unit contains a laser dichroic mirror that is of inferior quality to that used in the EQM and flight model, resulting in instrument sensitivity at 248 nm that is a factor of 60% worse. This dichroic, positioned at the center of the primary mirror of the Schmidt-Cassegrain telescope, is responsible for reflecting the laser light to project it to the rest of the telescope and out to the target and also for transmitting the returned plasma light to the optical fiber and spectrometers (Maurice et al., 2012). This degraded UV sensitivity in the LANL instrument is significant enough to affect the signal-to-noise ratio at 248 nm and could explain the slight preference in our work for the 778-nm O line over the 248-nm C line for normalization.

While all normalizations provide similar results for the relatively low hydration data examined here, our work also shows that the increase in normalized LIBS H signal with weight percent H may not be linear at high weight percent H. This effect was not observed in the smaller sample set considered by Rapin et al. (2017a) which covered a similar range (0–50 wt.% H₂O) but is apparent in our data (Figure 5). A linear relationship was not an a priori assumption of our study. Emission line intensity is expected to increase proportional to the number of emitting atoms, that is, their mole fraction. We also tested whether the measured H signal increases linearly for mole fraction H by calculating based on stoichiometry the mole

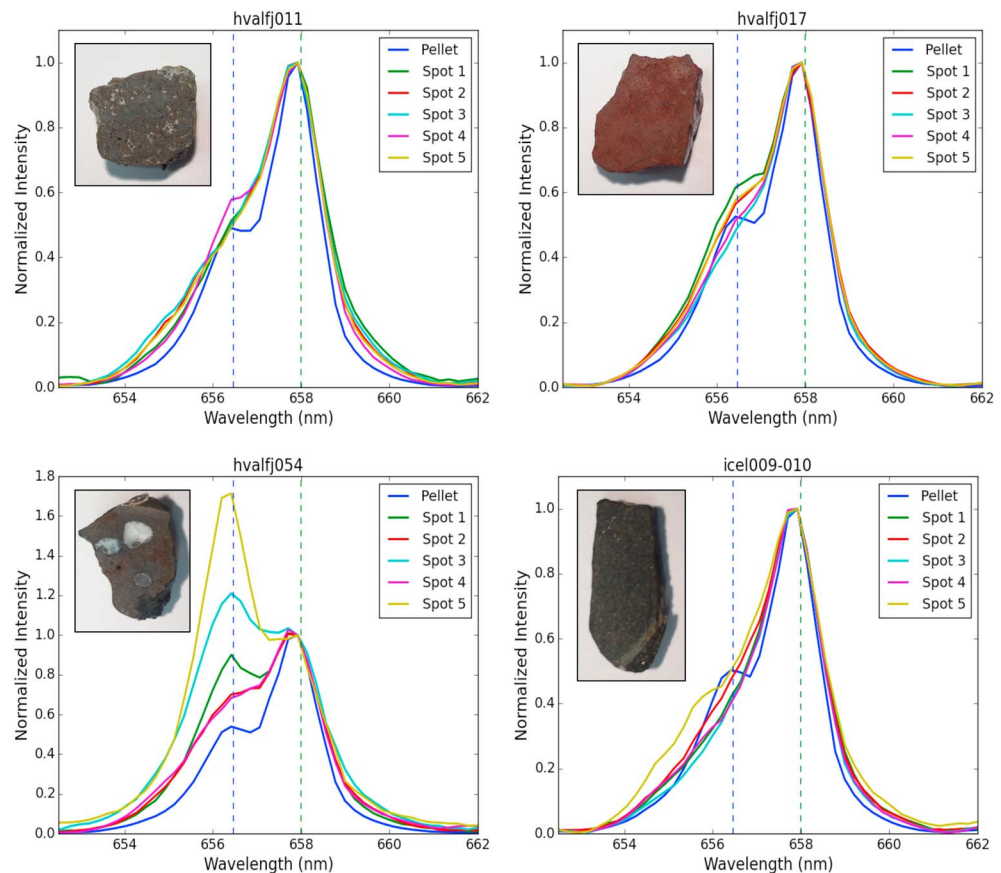


Figure 10. Physical matrix comparison. Laser-induced breakdown spectroscopy spectra normalized to the height of the C peak at 658 nm of pelletized (all five spots on the pellet were averaged) and rock chip samples from Iceland.

fraction H for three of our mixtures: brucite and K1919, gypsum and K1919, and gypsum and GBW07105, using the independent lab-derived chemistry of the basaltic endmembers (Figure A2). The gypsum points are complicated by probable water loss during chamber pump down (see section 3.2), but the brucite, even considered alone, markedly departs from linearity as a function of mole fraction H too. Some of the other nonlinear trends seen in Figure 4, like those for Fe sulfate, could be accounted for by the influence of the adjacent Fe peak, which may not fully be accounted for in peak fitting. On the other hand, alunite and Mg sulfate (and Fe sulfate) also show a nonlinear increase with weight percent, in a way that would only be accentuated if our estimates for their H content are overestimates (due to loss during chamber pump down). Our hypothesis is that the nonlinearities at high H contents are due to chemical matrix effects because the addition of the hydrated material at high levels changes the average makeup of the sample. Nonlinearity could affect our ability to predict weight percent H for very hydrated ChemCam (or SuperCam) targets on Mars. This is an important regime that requires further study, including more high H samples to extend and improve the calibration at $> \sim 1.25$ wt.% H or $> \sim 11$ wt.% H_2O . Multivariate methods may be required.

Finally, our study highlights two additional factors that affect H peak calibration curves but are not yet completely understood. First, the range of shot numbers used will very clearly affect the calibration curve (Figure 7). The higher the shot number, the shallower the calibration curve. This may be due to dehydration of the sample by the laser or due to simple cavity effects (Rapin et al., 2017b). Regardless, the implication for Martian data is clear: Calibration curves should only be used for the same shot number range they were initially determined with. Second, the distance to the target impacts the observed H signal. Normalizations to O 778 nm and C 248 nm best correct for distance and other differences in experimental conditions as seen in Figure 4 where the 100% gypsum samples plot closest together and in Figure 12, which shows the ratio of the LIBS H values for the same samples measured at different distances and in different

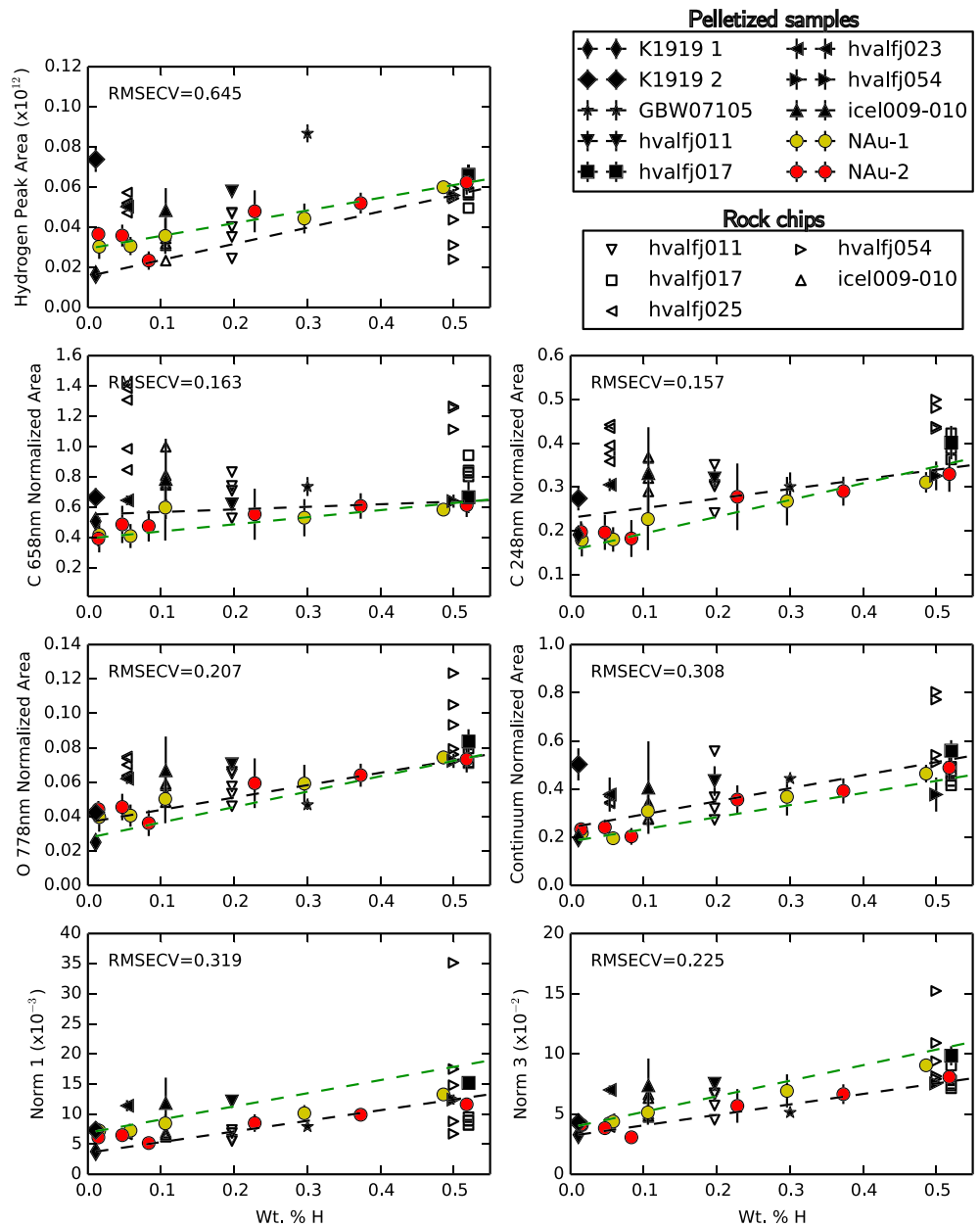


Figure 11. Hydrogen emission peak area versus weight percent hydrogen (calculated from temperatures $>150^\circ\text{C}$) for the basalt samples and the nontronite mixtures. Rock chip measurements are shown with open symbols, and pelletized samples are shown with solid symbols. A linear fit to the solid points (pelletized samples and nontronite mixtures) is shown here in black with RMSECV. The green dashed line is the best linear fit to all the samples in Figure 5 for comparison. The x axis error bars are >0.2 wt.% H and were removed for clarity. Trend line coefficients are included in Table A1. RMSECV = root-mean-square error cross-validation.

batches. But there is scatter in all normalizations for distance that indicate the effect of distance to target too could benefit from further laboratory analysis.

4.2. Physical Matrix Effects and Pellets Versus Natural Rocks

Rapin et al. (2017a) considered pressed pellets of lab mixtures, and here we also include natural samples, including rock chips to observe some of the complicating physical matrix effects and the challenges associated with measuring changes in LIBS H emission. Changes in grain size, cohesion, and sample roughness impact the shape of the H peak and the strength of H emission (Rauschenbach et al., 2008). Schröder

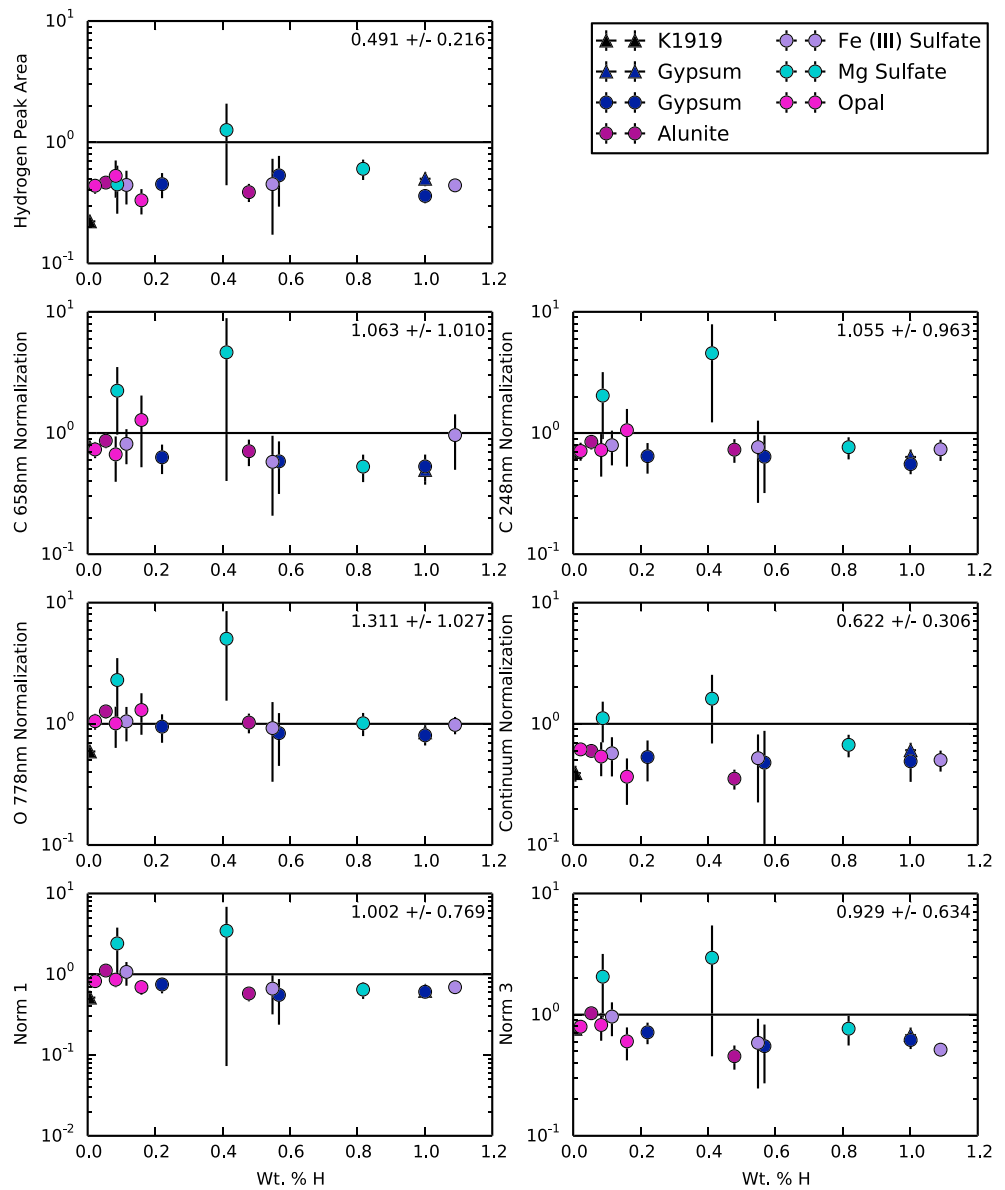


Figure 12. Ratios of peak areas taken from the same sample at different times as a function of weight percent H to show the effect of normalization on changes in experimental conditions. The triangles are the ratio of batch 1 (September 2013) laser-induced breakdown spectroscopy measurements to batch 2 (September 2014) measurements. The circles are the ratio of batch 4 (January 2017) measurements to batch 2 (September 2014) measurements. The average and standard deviation of the hydrogen values are shown in the upper right corner.

et al. (2015) and Meslin et al. (2013) describe ChemCam measurements showing generally higher H emission from unconsolidated soil targets than from rock targets, which can be interpreted as a result of physical matrix effects. Figure 10 shows our comparison of rock chip and pressed pellet spectra for four of the Iceland samples. Both samples are fine grained, hard, coherent. Some variation in H peak height can be explained by obvious contributions from individual hydrated grains, such as the zeolite inclusions targeted in the hvalfj054 sample. However, peak shape also changes for pressed pellet versus natural rock for all samples, including the relatively homogeneous samples like icel009 and hvalfj017 (Figure 10). The pressed pellet spectra have H peaks with smaller FWHM than the rock chip spectra. The other peaks like the C peak at 658 nm do not change shape with pellet versus rock. It is difficult to understand the cause of the larger FWHM for the rock chip samples as they have both more cohesion and larger sample roughness than the

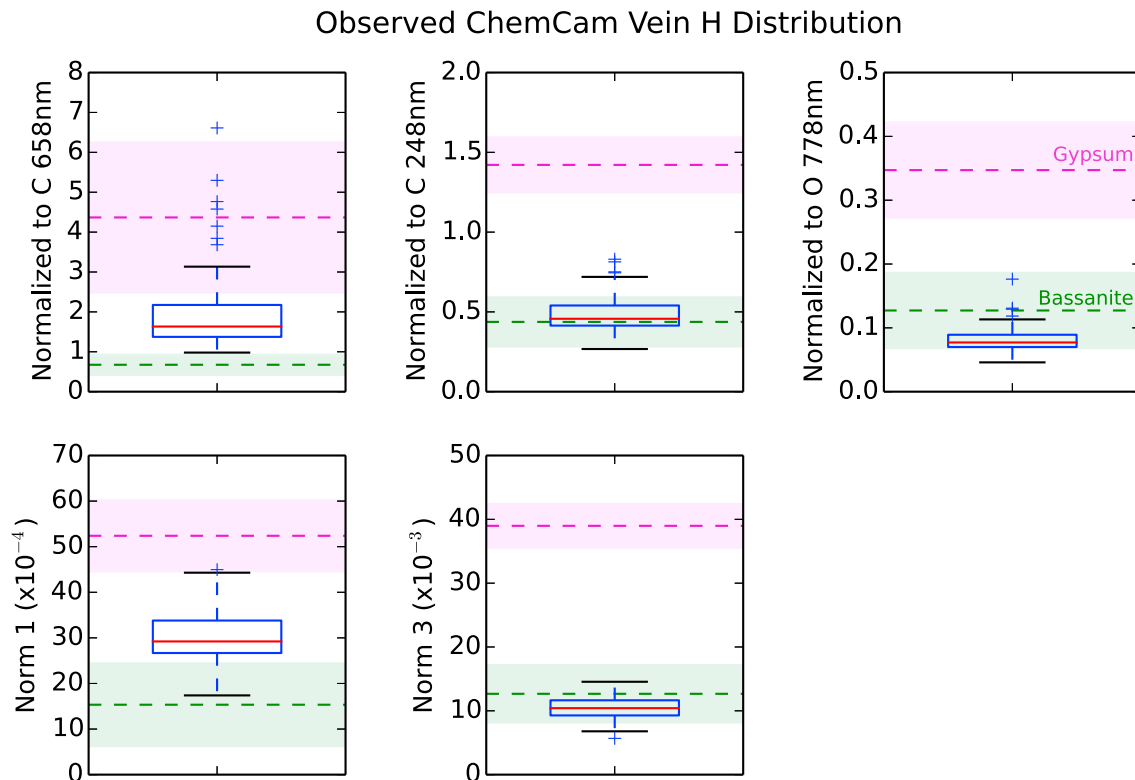


Figure 13. Boxplot of normalized H signal observed for ChemCam Ca sulfate vein points up to sol 1248. For comparison, we show the Figure 5 low range linear model predicted normalized H values for bassanite (6.2 wt.% H₂O, green) and polynomial model predicted values for gypsum (20.9 wt.% H₂O, magenta). The uncertainties, calculated using root-mean-square error as described in section 3.2, are represented as the shaded regions. The box extends from the lower to upper quartile values of the data, with a line at the median. The whiskers extend from the box to show the range of the data. Outlier points are defined as above or below 1.5 times the interquartile range from the median.

pressed pellets. The differences in FWHM are possibly caused by the documented Stark Effect for H (Kandel, 2009), which causes broadening of spectral lines.

The H calibration we have developed using the subset of pressed pellet mixtures (Figure 5, shown in green in Figure 11) mostly works for the natural pressed pellet samples and natural rock sample chips after normalization. The normalizations that performed well for the pelletized mixtures, normalization to C 248 nm, O 778 nm, and the continuum, also perform well for the pelletized natural samples. These normalizations bring the signal levels for the pelletized natural samples to levels comparable to the pelletized nontronite-basalt mixtures of similar water content. In these cases, the pelletized natural samples (shown with solid symbols) fall very close to the previous calibration trends shown in green, and the trend fit to the samples shown in Figure 11 is very similar. The rock chips (shown with open symbols) have higher variance in the measured LIBS H peak area because the targets are no longer homogenous at the LIBS spot scale of ~350 μm. Generally, we see an increasing trend in H peak area with weight percent H measured by TGA for all the rock chip samples for all normalizations (Figure 11). The normalizations that produce the most similar linear trends to the mixture pressed pellets again are the C 248-nm, O 778-nm, and the continuum normalizations. However, the C 658-nm normalization technique gives a normalized LIBS H signal that is the same within error for all four rock chip samples measured, suggesting that this normalization is not good for these rock chips. Collectively, the data suggest that the H content can be derived from LIBS measurements of natural samples for materials with similar matrices and physical textures. In the case of more chemically and physically homogeneous samples, like hvalfj017 and icel009-010, we expected the pellet trends to match the rock chip data more closely as we do see for the O 778-nm and C 248-nm normalizations within the uncertainties described in section 3.2. The shape differences in the H emission line and differences in derived H peak for pellet versus natural rock for the more heterogeneous natural samples suggest future work on rocks is needed to fully characterize texture or physical matrix effects.

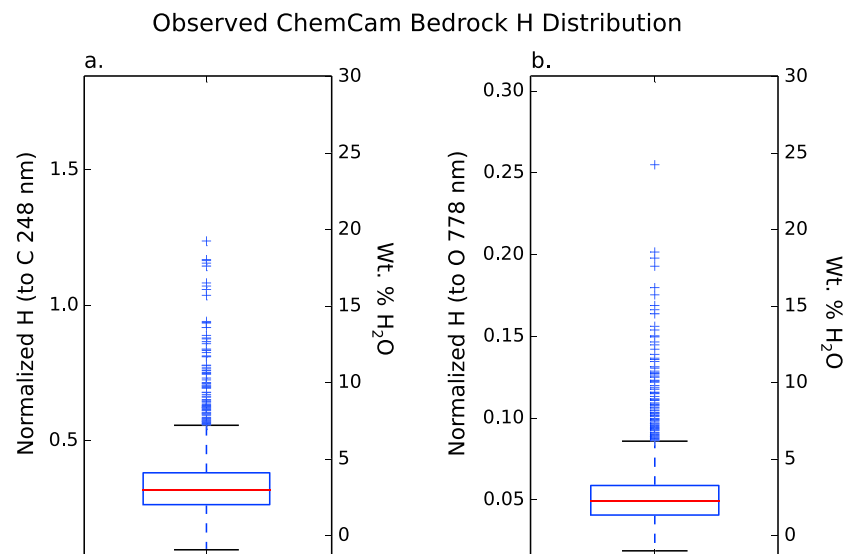


Figure 14. Boxplots of (a) C 248-nm and (b) O 778-nm normalized H signal observed for ChemCam Murray bedrock points (soils, veins, and clearly diagenetic textures removed) measured sols 766–1815. The box extends from the lower to upper quartile values of the data, with a line at the median. The whiskers extend from the box to show the range of the data. Outlier points are defined as above or below 1.5 times the interquartile range from the median.

4.3. Application to ChemCam and Future Applications

The ultimate goal of this work is to enable better ChemCam measurements of H on the Martian surface. Outside of Rapin et al. (2017a), other previous works such as Schröder et al. (2015) only present the detection of H and qualitative assessments of the amount of H present. Our application of the presented methods to ChemCam measurements of bedrock and Ca sulfate veins is only the second quantitative assessment of H using ChemCam and a first step showing the degree of uncertainty involved in applying this technique to identify specific mineral phases. As described in section 3.2, the amount of scatter in our laboratory data from the fit linear trend can be used to predict our level of certainty in ChemCam measurements.

Analysis of the sulfate veins in the Mars ChemCam data show that the choice of normalization does not change the phase we identify when distinguishing mineral hydration state when the phases are relatively pure in veins (Figure 13). The interpretation of bassanite (versus gypsum) is robust in all normalizations. The few weight percent H₂O variability in the Martian data from different veins is comparable to the weight percent differences when applying different calibrations from the lab to Mars data. Direct comparison of sample hydration across targets with similar surface properties (cohesion, surface roughness, and grain size) is possible with normalization. For this reason, we compare the H values observed for homogeneous, smooth Murray bedrock targets and show most observation points have small amounts of water, <7.0 wt.% H₂O (Figure 14), comparable to the altered Icelandic basalts. The absolute water content of a rock is slightly affected by the choice of the normalization method (Figure 14), with the mean value for Murray bedrock ranging from 2.3 to 3.0 wt.% H₂O depending on the normalization method used. These ranges are similar to measurements by the SAM instrument of several drilled samples (0.9 ± 0.3 to 2.5 ± 1.6 wt.% H₂O; Sutter et al., 2017) and measurements of the drier top layer by the DAN instrument (0.5 to 2.0 wt.% WEH; Mitrofanov & Litvak, 2015). The high outlier points are isolated occurrences of high weight percent H₂O in visibly unaltered Murray bedrock, which could represent mixing with hydrated Ca sulfate or phyllosilicates phases. Overall, these data indicate that the water content of samples can be successfully estimated using normalized univariate analyses of H peak area in ChemCam data.

Ultimately, this laboratory study better informs both future ChemCam studies of hydration as well as future SuperCam studies. The SuperCam instrument, part of the Mars 2020 mission, will have improved spectral resolution in the VNIR range, which will aid in distinguishing the H and C 658-nm emission lines as well as the Fe 654.8-nm and 659.4-nm lines. SuperCam's temporally gated intensifier will also aid in distinguishing between peaks as well as boosting signal, and its infrared spectroscopy and Raman subsystem will also help to decipher the possible contributors to the LIBS H signal (Wiens et al., 2017).

5. Conclusions

This study builds upon previous work by Rapin et al. (2017a) and others by measuring a wider variety of H-bearing materials, important for characterizing chemical and physical matrix effects and evaluating different normalizations for H determination on Mars. We prepared a sample set including both mixtures of minerals with known, systematic variation in hydrated mineral content and compositionally well-characterized altered volcanic rocks. TGA measurements allowed us to independently measure sample hydration. We find that

- Loss of sample water during chamber pump down to low pressure is a significant experimental effect that must be accounted for in any study involving hydrated/hydroxylated materials under Mars temperatures and pressures. It was successfully mitigated here by considering only water lost at temperatures $>150^{\circ}\text{C}$ and by emphasizing analyses of hydroxylated species, which are more stable, when constructing calibration curves with LIBS hydrogen peak area and weight percent H.
- Emission from H (I) 656.5 nm increases monotonically with both weight percent and mole fraction H for all the prepared mixtures except for opal and the natural altered basalts, where there is variance at low H weight percent.
- The H peak area increases linearly with weight percent H in the laboratory mixtures with structurally bound H for weight percent H up to about 1.25 wt.% H and then steepens for higher H-content samples, a potential nonlinear trend not noted by previous studies but important for correct characterization of high water content materials on Mars.
- The uncertainty in our ability to predict weight percent H from the LIBS H signal using the fit lines for the O 778-nm and C 248-nm normalizations ranged between ± 0.18 and 0.43 wt.% H. We calculate and observe visually a limit of detection of 0.4–0.9 wt.% H_2O for the C 248-nm and O 778-nm normalizations.
- Normalization to C 248 nm and O 778 nm are favored because they have lowest RMSECV trends and best correct for distance and other experimental effects in the laboratory data. C (I) 248 nm was favored by Rapin et al. (2017a); we slightly prefer normalization to O (I) 778 nm because it is a neutral emission line on the same (VNIR) detector as H. When applied to ChemCam data on Mars both perform similarly and predict and variation in results depending on normalization method used is typically <0.1 wt.% H.
- Comparison of sample hydration across different physical matrices is challenging because sample properties like surface roughness, cohesion, and grain size impact LIBS measurements of H. The natural samples we measured as both rock chips and pressed pellets document the effects of physical matrix on H emission, especially on the H peak shape even though these samples are all hard, coherent, and fine grained. While the pelletized samples have H emission comparable to the measured nontronite samples, the rock chips show considerable, nonsystematic scatter relative to the best linear fit from our mixtures that is not obviously solely due to compositional variation. Future work is needed to characterize these physical matrix effects for natural rocks.

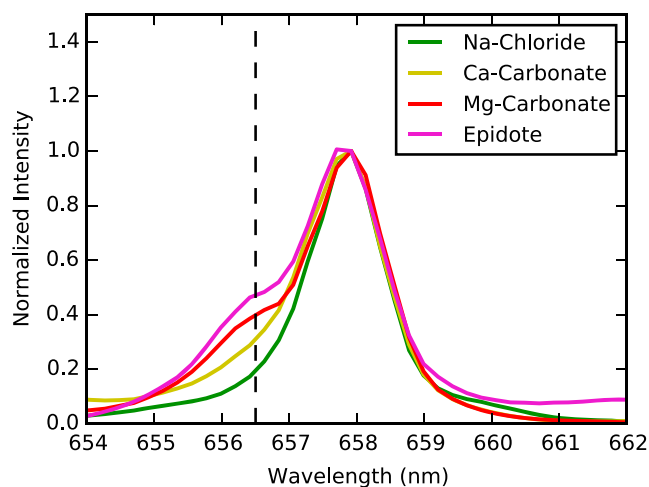


Figure A1. Comparison of samples with low measured weight percent H for determination of the H peak detection limit including Na chloride (0 wt.% H), Ca carbonate (0.01 wt.% H), Mg carbonate (0.1 wt.% H), and epidote (0.09 wt.% H).

These results are applicable to both MSL ChemCam and the Mars 2020 SuperCam instrument. While quantitative measurements of H in Martian samples are challenging due to matrix effects, qualitative comparison of H across targets with similar surface properties is possible and provides reasonable estimates of the weight percent H_2O in the Martian bedrock independently measured by the SAM and DAN instruments. This allows us to track changes in bedrock hydration throughout Curiosity's traverse.

Appendix A

Additional information supporting the main text is provided here. Spectra of samples with low wt. % H showing the detection limit are included in Figure A1. The effect of using mol fraction H versus wt. % H on the linearity of normalized calibration curves is shown in Figure A2. Figure A3 shows the normalization quantities, or denominators, used in Figure 4. The fit coefficients for the linear and polynomial trend lines shown in Figures 4, 5, and 12 are included in Table A1.

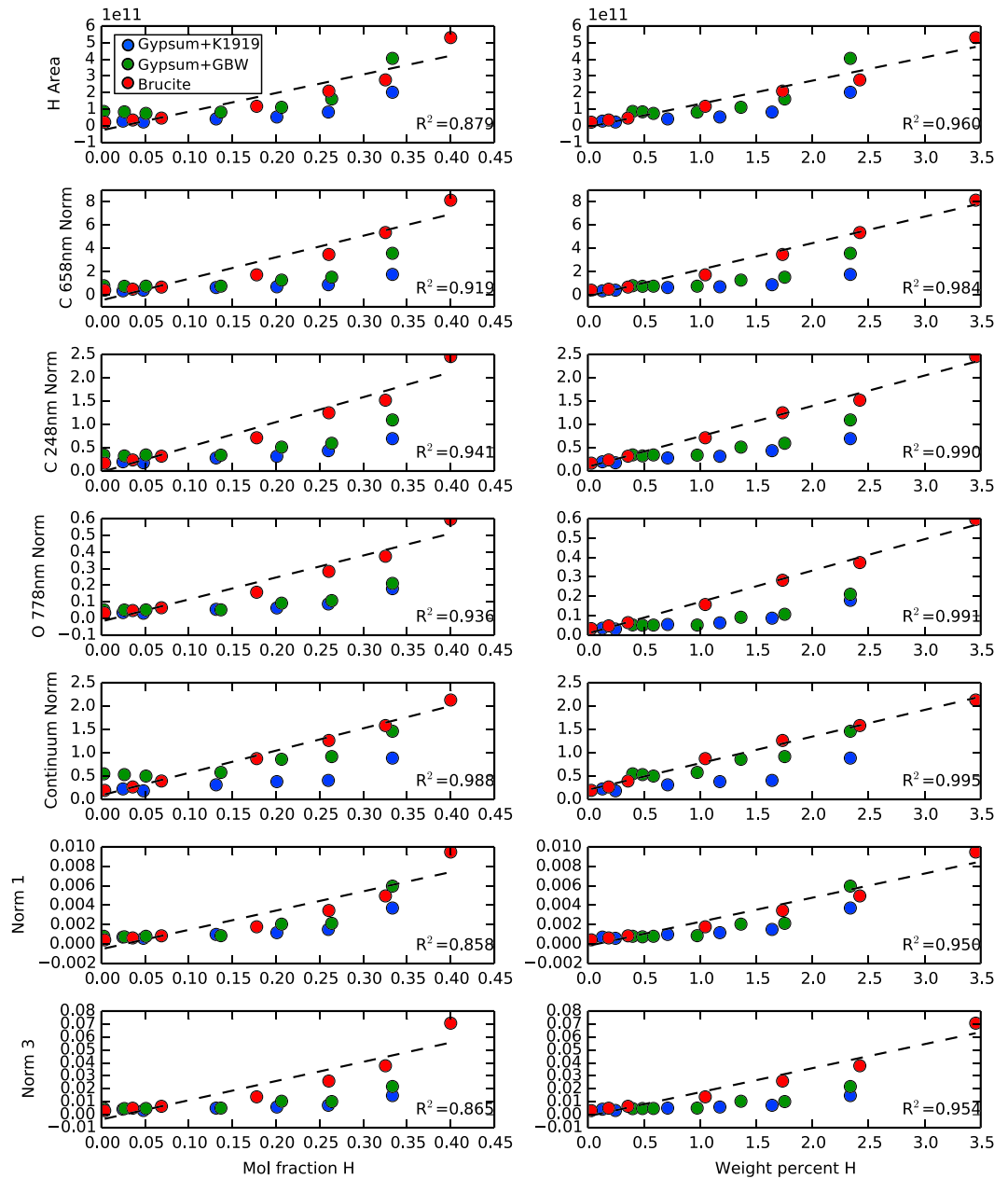


Figure A2. Calculated H peak area, unnormalized and for all normalization methods, shown as a function of (a) the theoretical mole fraction H (calculated from mineral stoichiometry) or (b) the actual measured weight percent H from thermogravimetric analysis. The best linear fit to the brucite mixture is shown with a black dashed line along with the R^2 value.

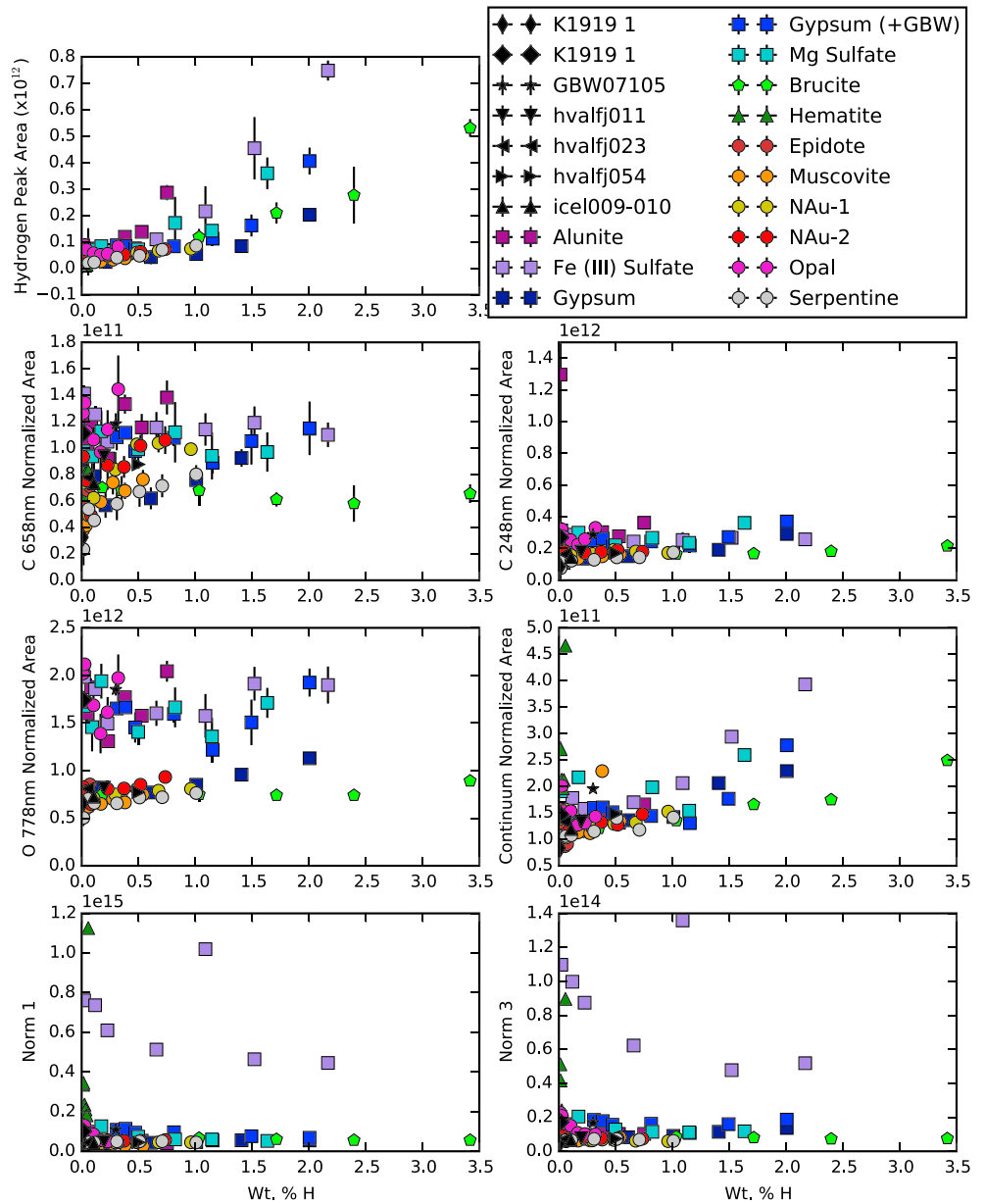


Figure A3. Hydrogen emission peak area versus weight percent H as shown in Table 2 for all samples. For all normalizations in Figure 4, we plot the denominator values that represent the value we are normalizing the first plot by.

Table A1
Coefficients for the Linear ($ax + b$) and Polynomial ($ax^2 + bx + c$) Trend Lines Shown in Figures 4, 5, and 12

	Normalization	Linear (all)		Linear (<1.25 wt.% H)		Polynomial		
		<i>a</i>	<i>b</i>	<i>a</i>	<i>b</i>	<i>a</i>	<i>b</i>	<i>c</i>
Figure 4	Hydrogen peak area	3.73E+10	1.59E+10	4.37E+10	1.58E+10	4.89E+10	1.04E+10	4.02E+10
	C 658-nm normalization	7.20E-01	4.15E-01	5.36E-01	4.35E-01	6.30E-01	1.26E-01	4.59E-01
	C 248-nm normalization	3.68E-01	1.79E-01	2.49E-01	1.91E-01	1.56E-01	1.31E-01	1.99E-01
	O 778-nm normalization	7.48E-02	3.03E-02	5.87E-02	3.15E-02	3.49E-02	3.58E-02	3.27E-02
	Norm 1	6.00E-04	3.69E-04	7.47E-04	3.67E-04	2.75E-04	8.25E-04	5.31E-04
	Norm 3	4.32E-03	3.23E-03	1.09E-02	2.80E-03	3.34E-03	1.20E-03	3.80E-03
	Continuum normalization	5.70E-01	1.90E-01	6.77E-01	1.84E-01	-3.57E-03	5.78E-01	1.89E-01
Figure 5	Hydrogen peak area	1.47E+11	2.80E+10	8.65E+10	2.90E+10	3.01E+10	4.35E+10	2.36E+10
	C 658-nm normalization	8.62E-01	3.67E-01	6.14E-01	3.88E-01	6.16E-01	2.48E-01	4.08E-01
	C 248-nm normalization	5.05E-01	1.49E-01	3.06E-01	1.65E-01	1.32E-01	2.25E-01	1.70E-01
	O 778-nm normalization	1.23E-01	2.58E-02	8.36E-02	2.82E-02	2.85E-02	6.91E-02	2.88E-02
	Norm 1	2.57E-03	6.85E-04	1.04E-03	7.09E-04	5.06E-04	8.14E-04	5.59E-04
	Norm 3	1.96E-02	3.79E-03	9.56E-03	3.94E-03	3.91E-03	6.03E-03	3.45E-03
	Continuum normalization	5.44E-01	1.80E-01	4.48E-01	1.86E-01	3.74E-02	4.43E-01	1.86E-01
Figure 12	Hydrogen peak area	8.07E+10	1.55E+10					
	C 658-nm normalization	1.71E-01	5.50E-01					
	C 248-nm normalization	2.19E-01	2.30E-01					
	O 778-nm normalization	7.20E-02	3.67E-02					
	Norm 1	1.77E-03	3.58E-04					
	Norm 3	8.70E-03	3.19E-03					
	Continuum normalization	5.43E-01	2.40E-01					

Acknowledgments

We thank Mark Davis, from Caltech Chemical Engineering, and his lab group, in particular Kramer Brand and Marat Orazov, for assisting us in using their thermogravimetric analysis instrument. The authors gratefully recognize the work of Rhonda McInroy in collecting LIBS measurements at LANL. We also thank Agnes Cousin for helpful discussions. Thanks to George Rossman for help in sample selection, acquisition, and preparation. The work at Caltech was supported by a NASA MSL Participating Scientist Program grant to B. L. Ehlmann and a National Science Foundation Graduate Research Fellowship grant DGE-1144469 to N. H. Thomas. Work at LANL and the instrument facilities were supported by the NASA MSL project. O. F., P.-Y. M., J. L., O. G., and S. M. participation to MSL and ChemCam is supported by CNES. We would also like to acknowledge the assistance of the editors and two anonymous reviewers in improving this manuscript. All ChemCam data used in this paper are publicly available on the PDS. Some of our supporting data have been previously published in Anderson et al. (2017); all spectra are included as supporting information.

References

- Anderson, D. E., Ehlmann, B. L., Forni, O., Clegg, S. M., Cousin, A., Thomas, N. H., et al. (2017). Characterization of LIBS emission lines for the identification of chlorides, carbonates, and sulfates in salt/basalt mixtures for the application to MSL ChemCam data. *Journal of Geophysical Research: Planets*, 122, 744–770. <https://doi.org/10.1002/2016JE005164>
- Blake, D., Vaniman, D., Achilles, C., Anderson, R., Bish, D., Bristow, T., et al. (2012). Characterization and calibration of the CheMin mineralogical instrument on Mars Science Laboratory. *Space Science Reviews*, 170(1–4), 341–399. <https://doi.org/10.1007/s11214-012-9905-1>
- Campbell, J. L., Perrett, G. M., Gellert, R., Andruschenko, S. M., Boyd, N. I., Maxwell, J. A., et al. (2012). Calibration of the Mars Science Laboratory Alpha Particle X-ray Spectrometer. *Space Science Reviews*, 170(1–4), 319–340. <https://doi.org/10.1007/s11214-012-9873-5>
- Clegg, S. M., Sklute, E., Dyar, M. D., Barefield, J. E., & Wiens, R. C. (2009). Multivariate analysis of remote laser-induced breakdown spectroscopy spectra using partial least squares, principal component analysis, and related techniques. *Spectrochimica Acta Part B: Atomic Spectroscopy*, 64(1), 79–88. <https://doi.org/10.1016/j.sab.2008.10.045>
- Clegg, S. M., Wiens, R. C., Anderson, R., Forni, O., Frydenvang, J., Lasue, J., et al. (2017). Recalibration of the Mars Science Laboratory ChemCam instrument with an expanded geochemical database. *Spectrochimica Acta Part B: Atomic Spectroscopy*, 129, 64–85. <https://doi.org/10.1016/j.sab.2016.12.003>
- Ding, Z., & Frost, R. L. (2002). Controlled rate thermal analysis of nontronite. *Thermochimica Acta*, 389(1–2), 185–193. [https://doi.org/10.1016/S0040-6031\(02\)0059-X](https://doi.org/10.1016/S0040-6031(02)0059-X)
- Ehlmann, B. L., Bish, D. L., Ruff, S. W., & Mustard, J. F. (2012). Mineralogy and chemistry of altered Icelandic basalts: Application to clay mineral detection and understanding aqueous environments on Mars. *Journal of Geophysical Research*, 117, E00J16. <https://doi.org/10.1029/2012JE004156>
- Ehlmann, B. L., & Edwards, C. S. (2014). Mineralogy of the Martian surface. *Annual Review of Earth and Planetary Sciences*, 42(1), 291–315. <https://doi.org/10.1146/annurev-earth-060313-055024>
- Földvári, M. (2011). *Handbook of thermogravimetric system of minerals and its use in geological practice* (p. 213). Budapest: Occasional Papers of the Geological Institute of Hungary.
- Gasnault, O., Mazoyer, J., Cousin, A., Meslin, P.-Y., Lasue, J., Lacour, J. L., et al. (2012). Deciphering sample and atmospheric oxygen contents with ChemCam on Mars. In Lunar and Planetary Science Conference (p. 2888). <https://doi.org/10.1007/s00216-011-4747-3>.
- Hadnott, B. A., Ehlmann, B. L., & Jolliff, B. L. (2017). Mineralogy and chemistry of San Carlos high-alkali basalts: Analyses of alteration with application for Mars exploration. *American Mineralogist*, 102(2), 284–301. <https://doi.org/10.2138/am-2017-5608>
- Kandel, Y. P. (2009). *An experimental study of H Balmer Lines in pulsed laser plasma*. Middletown, CT: Wesleyan University.
- Keeling, J. L., Raven, M. D., & Gates, W. P. (2000). Geology and Characterization of Two Hydrothermal Nontronites from Weathered Metamorphic Rocks at the Uley Graphite Mine, South Australia. *Clays and Clay Minerals*, 48(5), 537–548. <https://doi.org/10.1346/CCMN.2000.0480506>
- Kurniawan, K. H., Tjia, M. O., & Kagawa, K. (2014). Review of laser-induced plasma, its mechanism, and application to quantitative analysis of hydrogen and deuterium. *Applied Spectroscopy Reviews*, 49(5), 323–434. <https://doi.org/10.1080/05704928.2013.825267>
- Lazic, V., & De Ninno, A. (2017). Calibration approach for extremely variable laser induced plasmas and a strategy to reduce the matrix effects in general. *Spectrochimica Acta Part B: Atomic Spectroscopy*, 137, 28–38. <https://doi.org/10.1016/j.sab.2017.09.001>
- Mahaffy, P. R., Webster, C. R., Cabane, M., Conrad, P. G., Coll, P., Atreya, S. K., et al. (2012). The sample analysis at Mars investigation and instrument suite. *Space Science Reviews*, 170(1–4), 401–478. <https://doi.org/10.1007/s11214-012-9879-z>

- Maurice, S., Clegg, S. M., Wiens, R. C., Gasnault, O., Rapin, W., Forni, O., et al. (2016). ChemCam activities and discoveries during the nominal mission of the Mars Science Laboratory in Gale crater, Mars. *Journal of Analytical Atomic Spectrometry*, *31*(4), 863–889. <https://doi.org/10.1039/C5JA00417A>
- Maurice, S., Wiens, R. C., Saccoccio, M., Barraclough, B., Gasnault, O., Forni, O., et al. (2012). The ChemCam instrument suite on the Mars Science Laboratory (MSL) rover: Science objectives and mast unit description. *Space Science Reviews*, *170*(1–4), 95–166. <https://doi.org/10.1007/s11214-012-9912-2>
- Meslin, P.-Y., Gasnault, O., Forni, O., Schröder, S., Cousin, A., Berger, G., et al. (2013). Soil diversity and hydration as observed by ChemCam at Gale crater, Mars. *Science*, *341*(6153), 1,238,670–1,238,670. <https://doi.org/10.1126/science.1238670>
- Milliken, R. E., & Mustard, J. F. (2005). Quantifying absolute water content of minerals using near-infrared reflectance spectroscopy. *Journal of Geophysical Research*, *110*, E12001. <https://doi.org/10.1029/2005JE002534>
- Mitrofanov, I. G. and Litvak, M. L. (2015). Water and chlorine abundance along the traverse of Curiosity according to DAN measurements. In *Lunar and Planetary Science Conference* (p. 1423).
- Mitrofanov, I. G., Litvak, M. L., Varenikov, A. B., Barmakov, Y. N., Behar, A., Bobrovitsky, Y. I., et al. (2012). Dynamic Albedo of Neutrons (DAN) experiment onboard NASA's Mars Science Laboratory. *Space Science Reviews*, *170*(1–4), 559–582. <https://doi.org/10.1007/s11214-012-9924-y>
- Morris, R. V., Vaniman, D. T., Blake, D. F., Gellert, R., Chipera, S. J., Rampe, E. B., et al. (2016). Silicic volcanism on Mars evidenced by tridymite in high-SiO₂ sedimentary rock at Gale crater. *Proceedings of the National Academy of Sciences*, *113*(26), 7071–7076. <https://doi.org/10.1073/pnas.1607098113>
- Nachon, M., Clegg, S. M., Mangold, N., Schröder, S., Kah, L. C., Dromart, G., et al. (2014). Calcium sulfate veins characterized by ChemCam/Curiosity at Gale crater, Mars. *Journal of Geophysical Research: Planets*, *119*, 1991–2016. <https://doi.org/10.1002/2013JE004588>
- Rampe, E. B., Ming, D. W., Blake, D. F., Bristow, T. F., Chipera, S. J., Grotzinger, J. P., et al. (2017). Mineralogy of an ancient lacustrine mudstone succession from the Murray formation, Gale crater, Mars. *Earth and Planetary Science Letters*, *471*, 172–185. <https://doi.org/10.1016/j.epsl.2017.04.021>
- Rapin, W., Meslin, P.-Y., Maurice, S., Vaniman, D., Nachon, M., Mangold, N., et al. (2016). Hydration state of calcium sulfates in Gale crater, Mars: Identification of bassanite veins. *Earth and Planetary Science Letters*, *452*, 197–205. <https://doi.org/10.1016/j.epsl.2016.07.045>
- Rapin, W., Meslin, P.-Y., Maurice, S., Wiens, R. C., Laporte, D., Chauviré, B., et al. (2017a). Quantification of water content by laser induced breakdown spectroscopy on Mars. *Spectrochimica Acta Part B: Atomic Spectroscopy*, *130*, 82–100. <https://doi.org/10.1016/j.sab.2017.02.007>
- Rapin, W., Bousquet, B., Lasue, J., Meslin, P.-Y., Lacour, J.-L., Fabre, C., et al. (2017b). Roughness effects on the hydrogen signal in laser-induced breakdown spectroscopy. *Spectrochimica Acta Part B: Atomic Spectroscopy*, *137*, 13–22. <https://doi.org/10.1016/j.sab.2017.09.003>
- Rauschenbach, I., Lazić, V., Pavlov, S. G., Hubers, H.-W., & Jessberger, E. K. (2008). Laser induced breakdown spectroscopy on soils and rocks: Influence of the sample temperature, moisture and roughness. *Spectrochimica Acta Part B: Atomic Spectroscopy*, *63*(10), 1205–1215. <https://doi.org/10.1016/j.sab.2008.08.006>
- Schröder, S., Meslin, P.-Y., Cousin, A., Gasnault, O., Rapin, W., Blank, J., et al. (2014). Chemcam hydrogen detection in soils and dust along Curiosity's traverse. In *8th International Conference on Mars* (P. 1214).
- Schröder, S., Meslin, P.-Y., Gasnault, O., Maurice, S., Cousin, A., Wiens, R. C., et al. (2015). Hydrogen detection with ChemCam at Gale crater. *Icarus*, *249*, 43–61. <https://doi.org/10.1016/j.icarus.2014.08.029>
- Schröder, S., Rammelkamp, K., Vogt, D. S., Frohmann, S., Cousin, A., Gasnault, O., and Jubers, H.-W. (2018). Improving minor and trace element detection in Martian targets with time-resolved LIBS. In *Lunar and Planetary Science Conference* (p. 1962).
- Sobron, P., Wang, A., & Sobron, F. (2012). Extraction of compositional and hydration information of sulfates from laser-induced plasma spectra recorded under Mars atmospheric conditions—Implications for ChemCam investigations on Curiosity rover. *Spectrochimica Acta Part B: Atomic Spectroscopy*, *68*(Supplement C), 1–16. <https://doi.org/10.1016/j.sab.2012.01.002>
- Sutter, B., McAdam, A. C., Mahaffy, P. R., Ming, D. W., Edgett, K. S., Rampe, E. B., et al. (2017). Evolved gas analyses of sedimentary rocks and eolian sediment in Gale crater, Mars: Results of the Curiosity rover's sample analysis at Mars instrument from Yellowknife Bay to the Namib Dune. *Journal of Geophysical Research: Planets*, *122*, 2574–2609. <https://doi.org/10.1002/2016JE005225>
- Vaniman, D., Blake, D., Bristow, T., Marais, D. D., Achilles, C., Anderson, R., et al. (2013). Data from the Mars Science Laboratory CheMin XRD/XRF instrument. In *EGU General Assembly* (Vol. 15, p. 6272).
- Vaniman, D. T., & Chipera, S. J. (2006). Transformations of Mg- and Ca-sulfate hydrates in Mars regolith. *American Mineralogist*, *91*(10), 1628–1642. <https://doi.org/10.2138/am.2006.2092>
- Wiens, R. C., Maurice, S., Barraclough, B., Saccoccio, M., Barkley, W. C., Bell, J. F., et al. (2012). The ChemCam instrument suite on the Mars Science Laboratory (MSL) rover: Body unit and combined system tests. *Space Science Reviews*, *170*(1–4), 167–227. <https://doi.org/10.1007/s11214-012-9902-4>
- Wiens, R. C., Maurice, S., Lasue, J., Forni, O., Anderson, R. B., Clegg, S., et al. (2013). Pre-flight calibration and initial data processing for the ChemCam laser-induced breakdown spectroscopy instrument on the Mars Science Laboratory rover. *Spectrochimica Acta Part B: Atomic Spectroscopy*, *82*, 1–27. <https://doi.org/10.1016/j.sab.2013.02.003>
- Wiens, R. C., Maurice, S., & Rull Perez, F. (2017). The SuperCam remote sensing instrument suite for the Mars 2020 rover mission: A preview. *Spectroscopy*, *32*(5), 50–55.